Structure, materials and processes in the Earth's core and mantle

Véronique Dehant[1,2], Reidar G. Trønnes[3], Saioa A. Campuzano[4], Angelo De Santis[5], Wim van Westrenen[6]

[1] Royal Observatory of Belgium, email v.dehant@oma.be
[2] Université catholique de Louvain (UCLouvain)
[3] Natural History Museum and Center for Earth Evolution and Dynamics, Univ. of Oslo
[4] IGEO, Madrid, Spain
[5] Istituto Nazionale di Geofisica e Vulcanologia, Italy
[6] Vrije Universiteit Amsterdam, The Netherlands

Unpublished preprint, submitted to Surv. Geophys., May 10, 2021.
Later published as Dehant et al. 2022, Surv. Geophys. 43, 263–302, after major revisions, without RGT as co-author.
Total preprint length: 102 072 characters + spaces, incl. explanatory notes. Reference list: not included in the count.
RGT-text: 65 308 characters + spaces = 64.0 % of the text (+ the three first major figures, two of them deleted).

Contents

Abstract

This paper reviews current knowledge about the Earth's mantle and core in terms of structure, chemical and mineralogical compositions, and physical properties. High-pressure experimental techniques that can help to further constrain these properties and compositions are summarized, and the paper examines the consequences of core flows on variations in Earth's rotation and orientation as well as in the geodynamo. Finally, processes currently active at the core-mantle boundary (CMB) and the various coupling mechanisms between the core and the mantle are discussed, together with some evidence from magnetic field observations.

1. Mantle composition, structure and dynamics

1.1. Synopsis

Early in Earth's history, a deep silicate magma ocean and metallic protocore separated in a molten state at very high temperatures, driving the net chemical exchange equilibrium $2Fe^{metal} + SiO_2^{silicate} = Si^{metal} + 2FeO^{silicate}$ to the right. Therefore, the Fe-dominated protocore was Si-rich and the early magma ocean was FeO-rich. Subsequent planetary cooling reversed the equilibrium, setting the stage for extensive chemical exchange between the protocore and the magma ocean (MO), involving FeO transport from the MO to the core and SiO_2 in the opposite direction. The net transfer of SiO_2 out of the core is equivalent to the transfer of metallic Si to the magma ocean, resulting in immediate reduction of 2FeO to Fe, which is added to the core.

Due to the low Fe/Mg ratio in bridgmanite in equilibrium with coexisting MO melt, the earliest crystallization of $MgSiO_3$-dominated bridgmanite started at a neutral buoyancy level somewhere in the 1500-2200 km depth range. This separated the mantle into an upper MO, a middle crystalline shell and a basal magma ocean (BMO). The upper MO crystallized rapidly upwards from the bottom due to efficient heat loss to the surface, whereas the BMO became thermally insulated and crystallized slowly. Chemical BMO-core exchange continued during protracted BMO solidification, resulting in elevated Si/(Mg+Fe), Mg/Fe and bridgmanite/ferropericlase ratios in the middle and lower parts of the solidifying lower mantle. Crystallization of the MO and BMO therefore produced large volumes of refractory bridgmanite. The viscous nature of such material would have resulted in solid-state convective aggregation into Mm-sized domains, and most of these would have survived until the present day. The extent and duration of efficient BMO-core exchange, buffering the evolving BMO melt composition at high Si/(Mg+Fe) and Mg/Fe ratios, are uncertain. The very late-stage crystallization products (cumulates), however, are likely to have been FeO-rich and dense.

The continuous input of recycled oceanic crust (ROC) and lithosphere into the Earth's mantle started with deep subduction at about 3 Ga. Since then, a volume roughly estimated to be equivalent to 2.5 times the total mantle volume might have (re-)entered the mantle. Geochemical evidence from ocean island basalts indicates that ROC, sampled by deep-rooted mantle plumes, has been stored in different regions of the lowermost mantle for variable lengths of time, ranging from about 1.5 to 2.5 Gy. Seismically observable 5-40 km thick and variable ultra-low velocity zones (ULVZs), just above the core mantle boundary, may represent partially leaky "windows" between the present-day core and mantle. The ULVZs are thickest in the root-zones of deep plumes, which also sample tiny amounts of outer core metal, probably via the ULVZs.

1.2. Mantle composition

The bulk composition of the current mantle is commonly represented by pyrolitic models (term derived from the mineral names PYR-oxene[1] and OL-ivine[2]) based on the complementary relationship between melt-depleted peridotite[3] and basalt[4] identified in the 1960s (Ringwood, 1962a, 1962b; Green and Ringwood, 1963). Subsequently,

[1] Pyroxene general formula $XY(Si,Al)_2O_6$, where X is typically a mixture dominated by calcium, sodium, iron(II) or magnesium, and Y represents ions of smaller size, including mainly chromium, aluminium, iron(III), and magnesium.

[2] Olivine formula $(Mg, Fe)_2SiO_4$.

[3] Peridotite is the dominant mantle rock in terrestrial (Earth-like) planets, containing mainly olivine and pyroxene at low pressure and bridgmanite (about 75%), ferropericlase (20%) and Ca-perovskite (5%) at the conditions of the Earth's lower mantle.

[4] Basaltic magmas are formed by partial melting of peridotite at low pressure (near the Earth's surface). The oceanic crust has basaltic composition.

McDonough and Sun (1995) constructed more sophisticated compositional models of broadly "pyrolitic" compositions for the primitive mantle or bulk silicate Earth (BSE) by evaluating the chemical composition of numerous upper mantle (UM) peridotites[3] to identify the least melt-depleted samples, before adding an appropriate amount of a suitable partial melt. If a pyrolitic composition is representative for the primitive mantle, the fully molten magma ocean that formed in the aftermath of the Earth-Theia Moon-forming collision (and that coincided with the last episode of core segregation and metal-magma equilibration), was possibly also pyrolitic (e.g., Trønnes et al., 2019). An important question is whether the bulk mantle or the BSE is also pyrolitic. Alternatively, the BSE may tend towards a chondritic composition, characterized by an elevated Si/(Mg+Fe) ratio and therefore elevated pyroxene/olivine and bridgmanite[5]/ferropericlase[6] ratios in the upper and lower mantle, respectively. Several geochemical, mineral physical, seismic and geodynamic studies have concluded that the lower mantle (LM) might have an elevated Si/(Mg+Fe) ratio compared to the upper mantle (UM) and transition zone (TZ), containing domains enriched in bridgmanite (e.g., Murakami et al., 2012; Ballmer et al., 2017; Trønnes et al., 2019; Mashino et al., 2020).

1.3. Mantle structure, mineralogy and lithological density relations

The dominantly peridotitic mantle is divided into the UM, TZ and LM by seismic discontinuities at 410 and 660 km depth, caused by the phase transitions from olivine to wadsleyite[7] and from ringwoodite[8] to bridgmanite[5] + ferropericlase[6], respectively (e.g., Stixrude and Lithgow-Bertelloni, 2011, 2012; Irifune and Tsuchiya, 2015). Less distinct phase transitions at 520-540 km depth may result from the wadsleyite[7] to ringwoodite[8] transition and the stabilization of the minor Ca-perovskite phase (Deuss and Woodhouse, 2001; Saikia et al., 2008). The important TZ mineral, garnet[9], remains stable in the uppermost part of LM, but dissolves gradually into bridgmanite[5] with increasing pressure in the 660 to about 800 km depth range, causing a steep seismic velocity gradient in that range. Stixrude and Lithgow-Bertelloni (2011, 2012) and Irifune and Tsuchiya (2015) review the radial variation in average shear-wave velocity (V_S) and the mineral proportions for various lithological compositions (depleted peridotite, fertile or pyrolitic peridotite and basalt) throughout the mantle down to the CMB at 2891 km depth.

Equations of state for the LM minerals and density-depth profiles along an ambient mantle adiabat for the minerals and main lithologies are presented by Irifune and Tsuchiya (2015). Basaltic rocks, including eclogite[10] in the UM and garnetite[11] in the TZ, are denser than peridotite through most of the mantle, except for the 660-800 km depth range in the uppermost LM, where garnet, rather than the denser bridgmanite, remains stable. Ferropericlase[6] and high-pressure polymorphs of silica[12] (stishovite[13], β-stishovite and seifertite[15]) have the lowest and highest bulk moduli, respectively, of the LM minerals. Therefore, the density contrast between a denser silica-bearing basaltic rock and a ferropericlase-bearing peridotite, along an ambient adiabat decreases from 1.37 to 0.82 % with increasing pressure in the 40-110 GPa range, corresponding to the 1030-2440 km depth range, based on Irifune and Tsuchiya (2015) EoS (Equation of State) data. At 110 GPa and the ambient geotherm, the densities of basaltic, pyrolitic and harzburgitic[14] materials are 5381, 5331 and 5321 kg/m^3 respectively, compared to the PREM density of 5337 kg/m^3 (Dziewonski and Anderson, 1981). Beyond this pressure, the slightly densifying phase transitions from β-stishovite to seifertite[15] (at about 114 GPa along an ambient mantle adiabat) and from bridgmanite to post-bridgmanite complicate the density relations. The compositionally dependent bridgmanite to post-bridgmanite transition occurs at considerably shallower

[5] Bridgmanite is the Earth's most abundant mineral and has $MgSiO_3$ as the main component. With lesser amounts of the other components $FeAlO_3$, $FeSiO_3$ and $Al2O_3$, the simplest general formula can be expressed as (Mg,Fe)(Al,Si)O_3.
[6] Ferropericlase or magnesiowüstite is a solid solution between magnesium and iron oxide with the chemical formula (Mg,Fe)O.
[7] Wadsleyite is a high-pressure polymorph of olivine, $(Mg,Fe)_2SiO_4$, with the same general formula.
[8] Ringwoodite, a third $(Mg,Fe)_2SiO_4$ polymorph, is stable at higher pressures than wadsleyite. Olivine, wadsleyite and ringwoodite were previously referred to as the α, β (modified spinel) and γ (spinel) phases, respectively.
[9] Garnet has general formula $X_3Y_2(SiO_4)_3$, where X is divalent cations (Ca, Mg, Fe, Mn)$^{2+}$ and Y is trivalent cations (Al, Fe, Cr)$^{3+}$. In the deepest part of the upper mantle, through the transition zone and into the shallow part of the lower mantle, the garnet mineral assimilates pyroxenes to form an additional "majoritic" component with the simplest formula Mg_3 MgSi $(SiO_4)_3$.
[10] Eclogite is a moderate- to high-pressure form of basalt, stable at pressures of about 1-14 GPa.
[11] Garnetite is also a high-pressure form of basalt, dominated by garnet, and stable in the 14-30 GPa pressure range.
[12] Silica or silicon dioxide has the chemical formula SiO_2.
[13] Stishovite is a dense tetragonal polymorph of silicon dioxide.
[14] Harzburgite is an ultramafic rock, a variety of peridotite consisting mostly of olivine and low-calcium (Ca) pyroxene.
[15] Seifertite is one of the densest polymorphs of silica, a silicate mineral with the formula SiO_2.

level in basaltic or picritic rocks than in depleted peridotite. With a CMB temperature of 4000 K, the steep temperature gradients of 5-10 K/km through the thermal boundary layer of the D"-zone[16], which are very steep compared to the various mantle adiabats (plume adiabats to cold subducted slab adiabats) of about 0.3 K/km, will also variably affect the densities of the different lithologies. The main inference, however, is that recycled oceanic crust (ROC) of basaltic and picritic composition remains denser than depleted peridotite throughout the 740-2891 km depth range, even if the density contrast decreases with increasing depth (e.g., Ballmer et al., 2015; Torsvik et al., 2016).

Seismic tomography shows large lateral velocity variations in the UM, with slow regions under the mid-ocean ridges and subduction zones and fast regions under Archean cratons, suggesting heterogeneities in temperature and/or composition. For the five different S-wave tomography models shown by Romanowicz (2003) and Lay (2015), the root-mean-square amplitudes for shear-wave velocities of 2.3-2.8 % in the 50-200 km depth range (reflecting the presence of these heterogeneities) decrease markedly to a level of 0.3-0.6 % in the entire 700-2500 km depth range (reflecting a reduced degree of compositional / thermal heterogeneity), before they increase to values of 0.8-1.6 % in the lowermost 300-400 km of the mantle. In contrast, the RMS maxima of 0.30-1.36 % at 50 km depth for the four P-wave models in Lay (2015) decrease to 0.25-0.34 at 660 km depth and slightly further to 0.15-0.29% in the 900-2891 km depth range. It is important to note the absence of any significant increase in the amplitude of the P-wave velocity variation in the lowermost mantle and that the strongly increasing amplitudes in the S-wave velocity variations are limited to the lowermost 300-400 km of the mantle. This region, referred to as the D" zone, coincides with the thermal boundary layer above the CMB, where temperatures increase strongly from an average mantle adiabat of about 2500 K at 2600 km depth (e.g., Stixrude et al., 2009) to a CMB temperature of about 4000 K. As described in sections 1.4-1.9, the D" zone with its distinct compositional domains combined with strong lateral gradients and contrasts in temperature, density and viscosity, are fundamentally important for deep Earth evolution and dynamics.

1.4. Large low S-wave velocity provinces (LLSVPs) and degree-2 convection pattern

The strong lateral V_S variation in the D"-zone defines two antipodal so-called large low shear-wave velocity provinces (LLSVPs): one under the Pacific Ocean and the other under the southwestern part of Africa and bordering parts of the Atlantic and Indian Ocean. These two provinces are separated by a high-velocity longitudinal belt centered relatively close to the 120 E and 70 W meridians, crossing Asia, Australia, Antarctica, the Americas and the Arctic. Figure 1 shows this pattern in the SMEAN tomography model (Becker and Boschi, 2002) at 2800 km depth.

The Earth's residual geoid (Hager et al., 1985; Hager and Richards, 1989; Steinberger and Torsvik, 2008, 2010; Burke and Torsvik, 2012) and free-air gravity (Ishii and Tromp, 1999) reveal a degree-2 mantle convection pattern with antipodal broad outflow columns above the two LLSVPs, combined with the wide longitudinal belt of sheet-like inflow (downwelling). Although plate tectonic reconstructions are uncertain prior to the Pangea assembly, it appears that subduction during the past 540 Ma has mostly been confined to this belt, and that periods of minor true polar wander have adjusted the rotational mass imbalance caused by subduction at relatively high latitudes (Torsvik et al., 2014; Torsvik, 2019). The degree-2 mantle convection pattern is further indicated by the net characteristics of plate tectonics. Conrad et al. (2013) recorded the locations of net divergence and convergence of the plates and found that two divergence poles at approximately 180^o were located above the LLSVPs and that two convergence poles between approximately 90^o from the divergence centers were above the high-V_S circumpolar (longitudinal) belt. Whereas the reconstructed divergence poles have been relatively stationary above the LLSVPs during the last 250 My, the convergence poles have moved over greater distances above the circumpolar belt. This quadrupole pole pattern therefore suggests that the large-scale degree-2 convection has been stable in this 250 My period. The inferred lateral flow regime in the D"-zone (Figure 1) is away from the longitudinal belt of inflow (downwelling) towards the LLSVP margins. The orientations of the D"-zone seismic anisotropy with $V_S^{horisontal} > V_S^{vertical}$ appear to confirm this flow pattern (Lynner and Long, 2014a, 2014b, 2014c; Ford and Long, 2015).

Seismic studies reveal that the LLSVP margins are relatively sharp and steeply inclined, at least locally (Thorne et al., 2004; Garnero and McNamara, 2008; McNamara, 2019). The increased RMS amplitudes of lateral V_S-variations in the lowermost 300 km compared to the rest of the deep mantle (Romanowicz, 2003; Lay, 2015) and recent seismic analysis

[16] The D" layer, occupying the lowermost 200 km of the lower mantle (at a depth of ~2700–2900 km) is layer that is compositionally different to the other parts of the lower mantle.

(Koelemeijer et al., 2018) indicate that they are probably thermochemical features with about 300 km thick base layers, with a density excess sufficiently large to resist destruction by thermal buoyancy over at least hundreds of millions of years. Free-air gravity (Ishii and Tromp, 1999) and tidal tomography (Lau et al., 2017) investigations suggest that the lowermost 200-300 km of the LLSVPs have density excesses of about 1.25% compared to the surrounding mantle. Assuming a corresponding temperature excess of 750 K and thermal expansion data from Wolf et al. (2015), Trønnes et al. (2019) estimated an intrinsic density excess of 2.2% and a matching bridgmanite composition containing 16 mol% of the combined Fe-components, $FeAlO_3$ and $FeSiO_3$. The bridgmanite of ambient depleted peridotite in the lower mantle contains about 2.3, 3.8, 0.6 and 93.3 mol% of the components $FeAlO_3$, $FeSiO_3$, Al_2O_3 and $MgSiO_3$, respectively.

Assuming an outermost core temperature of 4000 K, the 300-400 km thick thermal boundary layer above the core-mantle boundary (CMB) is characterized by a strong temperature increase of about 1500 K from the ambient mantle adiabat of about 2500 K at 2600 km depth (e.g., Stixrude et al., 2009; Trønnes et al., 2019). The presence of post-bridgmanite in the cooler, high-V_S regions of the D"-zone, combined with the overall high temperatures close to the CMB, is likely to reduce mantle viscosity by three to four orders of magnitude (e.g., Amman et al., 2010; Nakada and Karato, 2012; Dobson et al., 2019). Conceivably, the LLSVP base layer may also have low viscosity, e.g., in the form of basaltic to picritic ROC, containing post-bridgmanite. In that case, the stabilizing factor may be the degree-2 convection pattern itself, which in turn is linked to, and probably stabilized by, the Earth's rotation (Steinberger and Torsvik, 2008, 2010). Material with an appropriate density excess will be swept into the LLSVP root zones of the broad antipodal outflow creating the residual geoid heights (Figure 1). If the density excess is too high, the material will form a continuous thin layer across the entire CMB. If it is too low, it will be convectively dispersed. Dense bridgmanitic cumulate material with about 16 mol% of the Fe-components ($FeAlO_3$ and $FeSiO_3$, see above), may be stable relative to post-bridgmanite in the lower part of the hot LLSVP base layers. As discussed in section 1.6 below, such material possibly formed as late-stage cumulates during the crystallization of the basal magma ocean, and will have high strength and viscosity, and thereby intrinsic stability.

1.5. Ultra-low velocity zones (ULVZs) feeding deep-rooted mantle plumes

Further contributions to the heterogeneity and material property gradients of the D"-zone are made by thin (5-40 km thickness) and laterally patchy ultra-low velocity zones (ULVZs) in direct contact with the CMB (Figure 2). The V_P and V_S reductions of about 10 and 30%, respectively, may indicate partial melt fractions of 5-10 % (e.g., Lay 2015). Several alternative (solid) material types, reviewed by McNamara (2019) and Trønnes et al. (2019), have been also been suggested as sources for these sharp decreases in seismic wave propagation speeds.

Most of the deep-rooted mantle plumes giving rise to large igneous provinces (LIPs) and ocean island basalt (OIB) appear to have developed and risen from sites along the LLSVP margins (e.g., Burke and Torsvik, 2004; Torsvik et al., 2006, 2010, 2016). The locations of 27 deep-rooted plumes from French and Romanowicz (2015) and 32 LIPs covering the 16-510 Ma age range, repositioned to their inferred original locations by Torsvik et al. (2021), relative to the LLSVP margins is shown in Fig. 1. Even kimberlites[17] with lower mantle geochemical features appear to be related to deep-rooted plumes in the general area of the African LLSVP, although their reconstructed eruption sites are not convincingly close the LLSVP-margins (Giuliani et al., 2021). The additional coincidence of ultra-low velocity zones (ULVZs) with the inferred plume sources along the LLSVP-margins (e.g., Thorne et al., 2004; Cottaar and Romanowicz, 2012; Yuan and Romanowicz, 2017) indicates that focusing of the lateral D" flow also tends to concentrate low-viscosity ULVZ-materials with density exceeding that of the LLSVPs into centers of columnar upwelling.

Subducted basaltic lithologies, which have solidus temperatures of about 3870 K at 130 GPa, are likely to undergo partial melting once they reach the hottest parts of the D"-zone near the LLSVP margins (e.g., Andrault et al., 2014; Pradhan et al., 2015; Baron et al., 2017; Tateno et al., 2018; Trønnes et al., 2019). In addition to the formation of dense silicate melt, Liu et al. (2016) found that a minor metallic melt fraction from the eutectic point on the Fe-C compositional join (about 2 wt% C; Fei and Brosh, 2014) would also be generated. The melting experiments of Andrault et al. (2014), Pradhan et al. (2015) and Tateno et al. (2018), demonstrate that Ca-perovskite is the first liquidus and last residual mineral in basaltic compositions in the lowermost mantle. The high density of residual Ca-perovskite

[17] Kimberlite is an igneous/magmatic rock formed at depth from anomalously enriched exotic mantle compositions and erupted rapidly and violently.

compared to lower-density seifertite (SiO_2) and $MgSiO_3$-dominated bridgmanite, would lead to differential sinking of the densest metallic melt, intermediate-density silicate melt and less dense Ca-perovskite crystals, combined with ascent of bridgmanite and seifertite. An Al-rich Ca-ferrite-structured mineral, also present in basaltic compositions in the lower mantle, would be melt-consumed at or near the solidus. Such a disaggregation of the partially melting basaltic material would concentrate sinking Ca-perovskite and interstitial melt into the underlying ULVZs. As pointed out by Hernlund and Jellinek (2010), the low viscosity of partially molten ULVZs is likely to induce sufficiently vigorous internal convection to prevent large-scale downwards segregation of the interstitial melt, keeping ULVZs seismically homogeneous (Lay 2015). A minor fraction of dense immiscible metallic melt, however, is likely to trickle downwards into the core, as it is continuously supplied from the melting of basaltic rock slivers passing laterally above. Diffusional extraction of the FeO-component from the silicate melt to the core and diffusional delivery of the SiO_2 component from the core to the ULVZs (see section 1.6), might reduce the density of the interstitial silicate melt to that of Ca-perovskite, or even less.

Therefore, the ULVZs may represent partially leaky "windows" between the D"-zone and the outer core. Such localized core-mantle exchange is supported by geochemical investigations of plume-related volcanic rocks. Recent isotopic measurements have revealed a negative correlation between the $^{182}W/^{184}W$ and $^{3}He/^{4}He$ ratios in major plume-related OIB suites (Mundl et al., 2017; Mundl-Petermeier et al., 2019, 2020; Rizo et al., 2019; Jackson et al., 2020). Radiogenic ^{182}W is derived from short-lived ^{182}Hf with a half-life of 9 My and has a practical lifetime of about 45 My, which implies extinction well before the Earth-Theia collision with resulting Moon formation. Because lithophile Hf partitions into silicate magma oceans while siderophile W partitions into metallic cores, the terrestrial planetary core material segregated early has very low $^{182}W/^{184}W$ ratio. Plumes giving rise to OIBs with low $^{182}W/^{184}W$ ratios are therefore likely to have sampled core metal, most likely via the ULVZs located in the plume root zones.

He-isotope systematics is a powerful tool to detect and characterize deep Earth domains that have remained relatively isolated and protected from convective destruction and mixing. Whereas ^{3}He is the primordial isotope, unaffected by radiogenic ingrowth, ^{4}He is continuously generated via the U and Th radioactive decay chains. Jupiter's gigantic H and He reservoir with a $^{3}He/^{4}He$ ratio of 120 times the ratio of the Earth's atmosphere (Mahaffy et al., 1998) is considered as the Solar system initial He-isotope composition, unaffected by radiogenic ^{4}He contributions. The highest ratio measured in plume basalts at Baffin Island and West Greenland (Starkey et al.; 2009; Mundl-Petermeier et al., 2019), representing extensive mantle melting within the starting Iceland plume head at 62 Ma and giving rise to the North Atlantic Igneous Province, is 50 times the atmospheric ratio. Because primordial-like high $^{3}He/^{4}He$ ratios are correlated with elevated plume flux (e.g., Jackson et al., 2017, 2021), the associated core-derived negative $^{182}W/^{184}W$ anomaly relative to Earth's common W isotope composition, suggests that mainly the most vigorous plumes are able to sample core metal entrained in the ULVZs. Although the primordial-like He composition conceivably also could be a core signal (e.g., Porcelli and Halliday, 2001; Porcelli and Elliott, 2008), it is more likely caused by the entrainment of more or less refractory bridgmanitic material into the plume conduit during transit through the lower mantle. Whereas Trønnes et al. (2018) suggested entrainment of very refractory BEAMS-material (see section 1.6) at mid-mantle depths to explain the primordial-like He-isotope signal, Jackson et al. (2020) and Giuliani et al. (2021) favor entrainment of more iron-rich magma ocean cumulates located at the base of the LLSVPs.

Additional Xe-isotopic evidence also points towards core metal contamination of the root-zones (presumably the ULVZs) of a more limited subset of deep-rooted plumes, in particular the Iceland plume. The strongest Xe-isotopic signal that can be ascribed to core contamination is recorded in Xe-rich fluid and melt inclusions in the Midfell subglacial eruption unit of the Western Rift Zone of Iceland, as well as in CO_2-dominated hydrothermal vents in the volcanic Eifel province in Germany (Harrison et al., 1999; White, 2015; Moreira et al., 2018; Jackson et al., 2018). A smoking gun for core contamination is a high $^{129}Xe/^{136}Xe$ ratio. Whereas ^{129}Xe is produced by the short-lived decay of ^{136}I (iodine) with half-life of 16 My, ^{136}Xe is a product of another short-lived fission decay of ^{244}Pu with 82 My half-life. Because siderophile I (iodine) and lithophile Pu are partitioned preferentially to the core and the magma ocean, respectively, the core would have acquired a high $^{129}Xe/^{136}Xe$ ratio (Jackson et al., 2018).

1.6. Magma ocean solidification and early refractory domains (ERDs)

Bridgmanite (bm) is the first liquidus phase in a wide range of peridotitic melts, from very refractory (depleted) to fertile (pyrolitic) and chondritic (i.e. bridgmanitic) compositions (Liebske and Frost, 2012; de Koker et al., 2013; Ozawa

et al., 2018). At pressures above 80 GPa, the bm-melt Fe/Mg exchange coefficient $K_D = (Fe/Mg)^{bm}/(Fe/Mg)^{melt}$ is 0.1 or even lower (e.g., Tateno et al., 2014). The very strong partitioning of Fe into melt compared to bridgmanite results in a bm-melt density crossover, with a neutral buoyancy level somewhere in the 1500-2200 km depth range in the early magma ocean (MO), following the Earth-Theia collision (Lock et al., 2018). In a rapidly rotating Earth, the early crystallization and accumulation of bm above and below this level might result in two hemispherical bm-shells penetrated by convective inflow along the polar axis and outflow in the equatorial plane, in analogy with the meridional flow in the Solar convective zone (Maas and Hansen, 2015, 2019; Gizon et al., 2020). Efficient cooling from above, with heat loss to space, might facilitate relatively rapid solidification of the outer MO (10-100 My scale) and the establishment of a long-lived basal MO (BMO).

The early crystallization of $MgSiO_3$-dominated and neutrally buoyant bm will be promoted and prolonged by the chemical exchange between the basal MO and protocore, involving the migration of FeO from the MO and subsequent BMO to the core and SiO_2 in the opposite direction. The basis for this exchange process is the net chemical exchange equilibrium $2Fe^{metal} + SiO_2{}^{silicate} = Si^{met} + 2FeO^{sil}$, which is driven to the right at the highest temperatures of final core segregation and reversed during subsequent planetary cooling (Malavergne et al., 2004; Tsuno et al., 2013; Laneuville et al., 2018). An important result of the chemical exchange and extensive bridgmanite crystallization is elevated Si/(Mg+Fe), Mg/Fe and bridgmanite/ferropericlase ratios of the lower mantle, compared to the bulk silicate magma ocean just after the main stage of core segregation. The early magma ocean, following core segregation in the aftermath of the Earth-Theia collision, is likely to have had an elevated Fe/Si ratio compared to a pyrolitic model composition (Trønnes et al., 2019), which is representative for the bulk convecting mantle, composed of more depleted peridotite and slivers of recycled oceanic crust.

The metal-silicate exchange equilibrium $2Fe^{metal} + SiO_2{}^{silicate} = Si^{met} + 2FeO^{sil}$ may also enhance the density stratification of the early MO and thereby promote bm-melt neutral buoyancy. Although some of the Theia core might have merged directly with Earth's core, the high-energy impact probably also resulted in considerable silicate-metal mixing and emulsification (e.g., Rubie et al., 2015). Subsequent cooling from above would establish a radial thermal gradient and result in the (re-)precipitation of sinking metal drops. The exothermic exsolution and sinking of heavy metal will promote the thermal gradient, driving the metal-silicate equilibrium towards the products, $Si^{met} + 2FeO^{sil}$, in the high-temperature, deepest parts of the magma ocean, and towards the reactants, $2Fe^{met} + SiO_2{}^{sil}$, in shallower regions with lower temperature. At an early post-collisional (Theia) stage, the strong density stratification caused by sinking metal drops and increasing FeO-content in the silicate melt with increasing depth, will inhibit thermal convection and enhance the buoyancy of early $MgSiO_3$-dominated bridgmanite crystals precipitating at a neutral buoyancy level. Subsequently, gradual cooling, even in the deepest parts of the BMO and outer core, causing transfer of SiO_2 from the core and FeO from the BMO to the core, will lead to thermal buoyancy of the deepest BMO, resulting in convection.

High-pressure phase relations indicate that the solidification of the magma ocean would have produced large amounts of early bridgmanite-dominated cumulates, as well as later bridgmanite-dominated residues from localized remelting above the basal magma ocean (e.g., Tateno et al., 2014; Ozawa et al., 2018; Caracas et al., 2019). Such viscous material, neutrally buoyant in the middle part of LM, can be convectively aggregated into bridgmanite-enriched ancient mantle structures, BEAMS (Manga, 1996a, 1996b; Ballmer et al., 2017), located outside the margins of rising mantle columns above the LLSVPs (Figs. 1-2). The schematic equatorial section (Figure 2) illustrates the locations of these inferred structural domains, the large-scale degree-2 mantle flow, as well as the inferred core flow, based on e.g., Trønnes (2010), Torsvik et al. (2014), Trønnes et al. (2019) and Olson (2016). As shown and described in Figure 1, we restrict the extent of the BEAMS relative to the original suggestion by Ballmer et al. (2017) in order to avoid interference (overlaps) with geologically reconstructed and seismically imaged slabs sinking through the lower mantle within the wide circumpolar belt of inflow (van der Meer et al., 2010, 2018). A definite seismic detection of BEAMS in the middle part of the lower mantle (Figs. 1-2), generally characterized by low seismic amplitudes, is challenging. However, the seismic signal of the crossover from high-spin to low-spin iron in ferropericlase (e.g., Kennett et al., 2021) appears to be relatively strong in the fastest and slowest regions of the lower mantle and weaker or absent in the intermediate regions where the BEAMS are likely positioned (Shephard et al., 2020). The existence of considerable amounts of neutrally buoyant, viscous and refractory bridgmanitic material in the lower mantle seems inescapable from a petrological and geodynamic point of view.

1.7. Primordial-like He and Ne isotopic compositions

In the hot Hadean Earth, rapidly diffusing He and Ne would recharge such U- and Th-depleted bridgmanitic material, mostly before its aggregation into Mm-sized BEAMS (Trønnes et al., 2018). Assuming a convective Urey-ratio of 0.29 from Jaupart et al. (2016) and the secular cooling curves of Herzberg et al. (2010), the average ambient mantle adiabat would be positioned 170-200 K above the present adiabat during the last 3-4 Ga. Under such thermal conditions, the diffusion rates for He and Ne are only sufficient to reset the isotopic compositions in bridgmanitic material within the outer 3-10 km rims of the Mm-sized BEAMS. Because the major plume conduits appear to be at least 500 km wide through the high-viscosity central part of the lower mantle (French and Romanowicz, 2015), they are likely able to erode and entrain material from considerably more than just the outer 10 km of the BEAMS.

It is important to note that neither the LLSVPs nor the ULVZs are suitable reservoirs for the primordial-like He and Ne isotopic compositions. The dense Ca-perovskite, which is likely to be a major ingredient in the ULVZs (see the section above), as well as in the LLSVPs, has extremely high concentrations of a range of large-ion lithophile elements, and especially U and Th (Hirose et al., 2004; Corgne and Wood, 2005; Corgne et al., 2005). The U and Th decay will produce radiogenic He and nucleogenic Ne, and therefore readily destroy any primordial-like He and Ne signal. Even the core appears to have too high U and Th content to preserve primordial-like He and Ne compositions (Faure et al., 2020). The reason that the LLSVP base layers are unsuitable, is that both of the two candidate materials (recycled oceanic crust and late-stage Fe-rich cumulates) are rich in Ca-perovskite. Suitable Fe-rich bridgmanite-dominated cumulates for the LLSVP base layers would have about 16 mol% combined of the two Fe-components $FeSiO_3$ and $FeAlO_3$ (Trønnes et al., 2019). Such bridgmanite has exactly the same density as Ca-perovskite, which is therefore expected to be enriched in the same cumulate layers.

1.8. Volume estimates for convecting mantle, subducted lithosphere and isolated mantle domains

The exact onset of plate tectonics is unconstrained, with recent estimates ranging between 3 and 4 Ga (e.g., Shirey and Richardson, 2011; Greber et al., 2017; Bauer et al., 2020). The transition from stagnant to mobile lid tectonics was probably gradual and quasi-episodic in the beginning (Korenaga, 2013). The earliest crustal reworking might have been quite shallow and in the form of Venus-type plume-related subduction (e.g., Gerya et al., 2015; Davaille et al., 2017; Sobolev and Brown, 2019), density-driven drip tectonics (Smithies et al., 2021) or Iceland-type crustal subsidence (Reimink et al., 2014). More familiar plate tectonics with deep subduction and recycling might have started at about 3 Ga (e.g., Shirey and Richardson, 2011). The input of subducted oceanic lithosphere into the convecting mantle during the 3-0 Ga period could potentially be estimated, based on the relation between oceanic lithosphere thickness and mantle potential temperature and secular cooling (e.g., Herzberg et al., 2010) if plate velocities and subduction rates were known accurately. The global volume flux variation of subducted oceanic lithosphere from 400 Ma to the present has been estimated by K.S. Karlsen (pers. comm.), based on seafloor age grids from plate tectonic reconstructions (Karlsen et al., 2020), plate velocities (Matthews et al., 2016) and oceanic lithosphere thickness (Parsons and Sclater, 1977). Although the variations are relatively large within shorter 20-50 My periods, the long-term trend involves decreasing volume flux from 400 Ma to the present. We derived a long-term trend by estimating the average volumes in eight 50 My bins (segments), followed by linear regression of these average volumes. The regressed volume flux, decreasing from 445 km^3/y at 400 Ma to 300 km^3/y today, was then scaled to the secular cooling trends of Herzberg et al. (2010), using a curve with a Urey ratio of 0.29 (Jaupart et al., 2016). Finally, we extended the scaled volume flux back to 3 Ga. The resulting cumulative volume of subducted lithosphere, which is 2.5 times the total mantle volume and 3.1 times the convective mantle volume (Figure 2 and next paragraph), may serve as a rough estimate of the rate of deep recycling in the Earth.

We can also derive rough estimates for the volumes of the mostly isolated mantle reservoirs. Based on Figs. 1 and 2, and by assuming an average thickness of 300 km for the LLSVP base layers, an average thickness of 100 km for the subcontinental lithospheric mantle (SCLM) and a continental surface fraction of 40%, we estimated the volumes of LLSVPs, BEAMS, SCLM and the remaining convective mantle to 1.1, 13.0, 2.3 and 83.6 % of the total mantle volume, respectively. The ULVZ volume is unknown, but considerably less than 10 % of the LLSVP base layer volume.

1.9. Storage site and age of recycled oceanic crust

The low viscosity of the D"-zone may facilitate partial density-driven separation of ROC lenses and slivers in the lateral D" flow above the CMB towards the LLSVP margins. The ROC lenses will preferentially be confined to the lower part of

the flow and possibly undergo partial melting and dense melt loss to the ULVZs, which are most abundant in the plume root-zones and focal areas for the lateral flow at the LLSVP margins (converging black arrows in Figure 1). When the flow is diverted upwards along the LLSVP margins, some of the residual ROC may have sufficient volume and density to be deposited and accumulated in piles on top of the LLSVP base layers, inwards from the margins (Torsvik et al., 2016; Trønnes et al., 2019). During storage in this area, which is sheltered from the most vigorous and focused mantle flow, the ROC will be heated conductively from the LLSVP base layer and from internal radioactive decay of U, Th and K. A partial approach towards neutral buoyancy for the heated and thermally expanding ROC pile material will promote its later entrainment in the pervasively rising mantle flow above the LLSVPs, as well as directly into vigorous plumes rising from the margins (or from the interior).

Geochemical evidence for the intermediate- to long-term storage of ROC material with associated sedimentary components entrained in modern oceanic island basalts (OIB) comes from their Pb-isotopic model ages. The average Pb model age of about 2 Ga corresponds to the slope of the Northern Hemisphere Reference Line (Hart, 1984; Jackson et al., 2020), whereas individual OIB volcanoes or entire islands record individual Pb-isotopic model ages in the 1.5-2.5 Ga range (Andersen et al., 2015). The sulfur isotopic composition of olivine-hosted sulfide inclusions in plume-derived basalts at Cook Island (Polynesia) indicate that Archean ROC, subducted during reduced surface conditions at the Earth, was entrained in some deep-rooted plumes (Cabral et al., 2013). The observation that each oceanic island seems to be characterized by a distinct and rather narrow Pb model age range indicates that the deep-rooted plumes might sample ROC accumulations of a distinct age range and compositions in different regions. The D"-zone has been suggested as the most likely storage site of dense ROC accumulations (Hirose et al., 2005; Torsvik et al., 2016; Ballmer et al., 2016; Thomson et al., 2019).

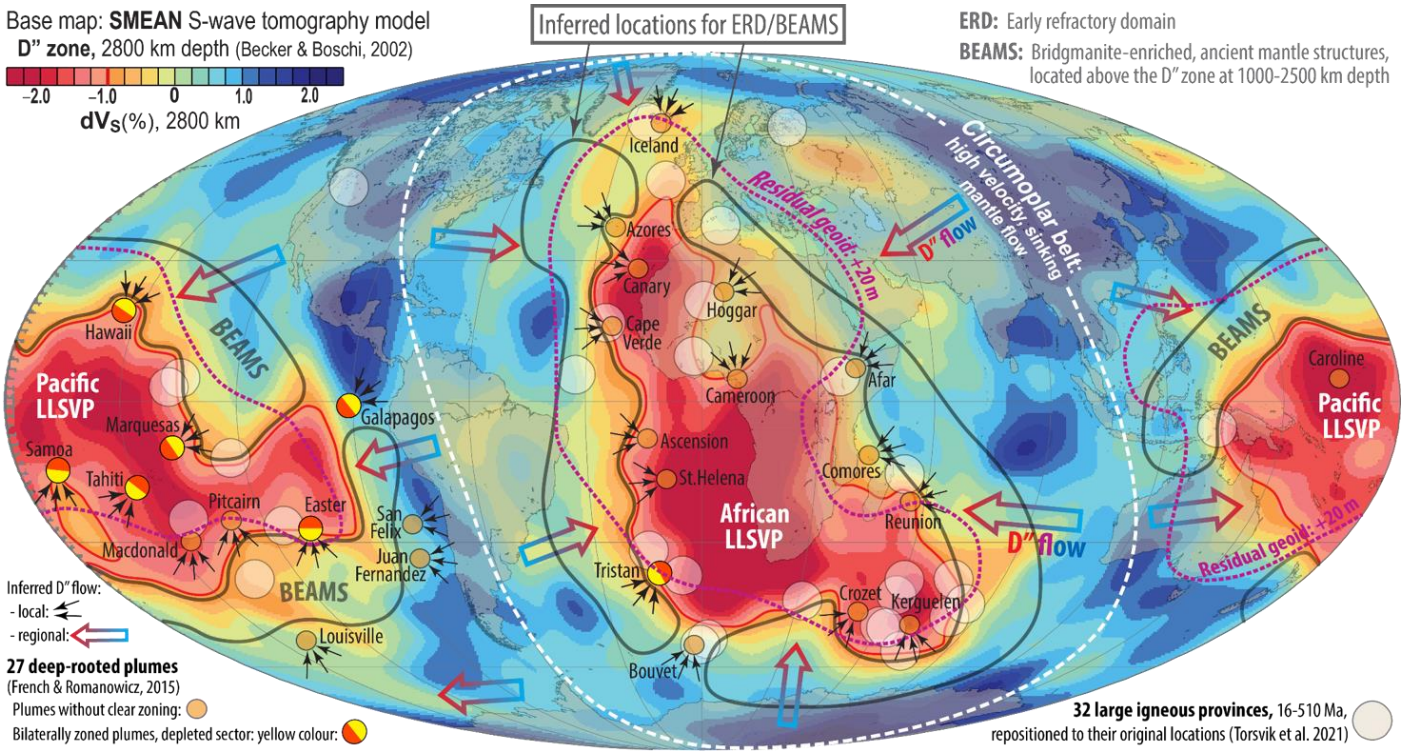

Figure 1. Base map with the SMEAN (mean S wave model from Becker and Boschi, 2002) mantle tomography model at 2800 km depth, showing the large low S-wave velocity provinces (LLSVPs), surrounded by a nearly longitudinal belt (60-90 W, 90-120 E) high-velocity belt, as well as the positions of 27 deep-rooted plumes from French and Romanowicz (2015) and 32 large igneous provinces, covering the 15-510 Ma range and relocated to their original eruption locations (Torsvik et al., 2021). The dV_S = -1% contours, marked by red lines on the SMEAN map, coincide with the largest lateral V_S gradients (Torsvik et al., 2006) and are therefore the best estimates of the LLSVP-margins. The LLSVPs projections at the Earth's surface correspond closely to the residual geoid highs, shown here by the +20 m contour (violet stippled lines) from Burke and Torsvik (2012). The residual geoid (total range of about 200 m) and the free-air gravity (Ishii and Tromp, 1999) demonstrate a large-scale degree-2 mantle convection pattern with antipodal broad outflow columns above the LLSVPs and inflow above the longitudinal (circumpolar) high-velocity belt. The inferred locations for highly viscous, early refractory domains or bridgmanite-enriched ancient mantle structures (ERD/BEAMS,

e.g., Ballmer et al., 2017; Trønnes et al., 2019), presumably confined to the 1000-2500 km depth range, are also projected onto the SMEAN map. In order to avoid interference (overlaps) with geologically reconstructed and seismically imaged slabs sinking through the lower mantle within the wide circumpolar belt of inflow (van der Meer et al., 2010, 2018), the inferred ERD/BEAMS are confined to narrow zones, peripheral to the supra-LLSVP outflow columns. The deepest of the reconstructed slabs, at 2700-2850 km depth, are approximately 250 My old.

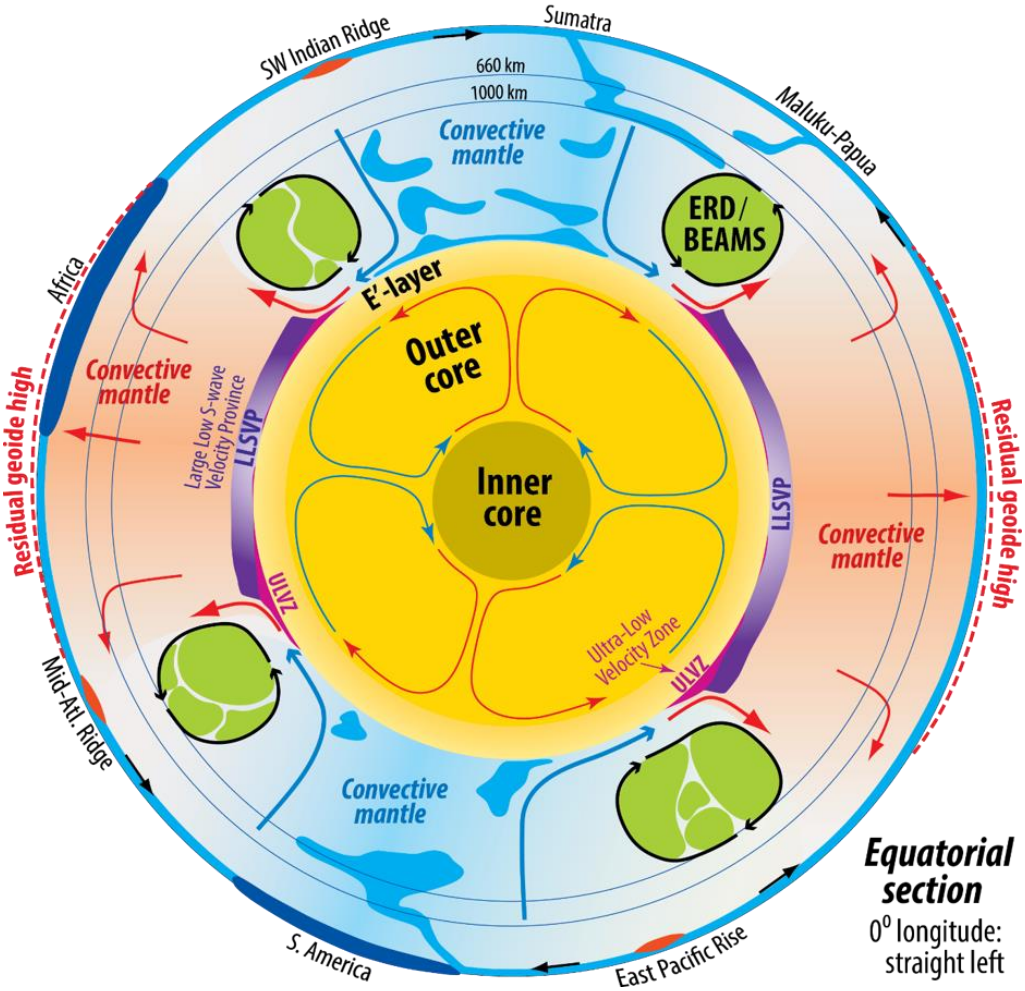

Figure 2. Approximate and schematic equatorial section showing Earth's main structural features and domains. ERD: Early refractory domains; BEAMS: bridgmanite-enriched ancient mantle structures. The section is constructed in accordance with Figure 1 and van der Meer et al. (2018, 2019).

2. Core composition, structure and dynamics

2.1. Synopsis

Very high temperatures during the exothermic processes of core metal exsolution and sinking through the silicate magma ocean into the growing protocore, would lead to elevated concentrations of Si in the protocore and FeO in the early silicate magma ocean (MO), according to the chemical exchange equilibrium $2Fe^{metal} + SiO_2^{silicate} = Si^{metal} + 2FeO^{silicate}$, which is driven towards the product (right) side with increasing temperature. Planetary cooling reverses the equilibrium, resulting in chemical exchange of SiO_2 from the core to the MO and FeO in the opposite direction. Due to the low diffusion rates of the major elements in ferropericlase, and especially in bridgmanite, this exchange becomes very restricted after the complete solidification of the basal MO (BMO). The main chemical evolution of the core during the exchange of oxides with the MO and BMO would have involved decreasing Si and increasing O contents. Even today when very limited exchange is possible, the core remains under-saturated with O.

An outer convecting iron-rich core with 5.5, 3.6 and 3.0 wt% Ni, Si and O, respectively, is broadly consistent with the density and velocity of the Preliminary Reference Earth Model (PREM). Replacing minor amounts of these elements with S, C and up to 0.1 wt% H would still fulfill the density and seismic velocity constraints. From a core depth of 445 km up to the core-mantle boundary (CMB), the seismic velocity decreases from the PREM value to about 0.43% below

the PREM curve (with the KHOMC model). This outermost E'-layer with an anomalous velocity gradient might be stable over a relatively long timescale, e.g., during the last 1-2 Gy. In spite of very low core metal viscosity, such a stagnant E'-layer with low density may be possible due to high thermal conductivity and low viscous entrainment, and it might have a stabilizing effect on the geodynamo. In order to explain the observed velocity reduction and an appropriate density reduction relative to a convecting core with about 3.6 wt% Si and 3.0 wt% O, recently published mineral physics data predict a density deficit of 0.98% and composition with 0.4 wt% Si and 6.7 wt% O near the CMB. Such a layer is fully consistent with core-BMO chemical exchange. Theoretical and experimental studies performed in the last decade indicate considerably higher thermal conductivity in the outer core liquid than in previous geodynamo models. Such high thermal diffusivity might stabilize a stagnant E'-layer and require a radioactive heat contribution and a high CMB heat flux to yield sufficient geodynamo power.

2.2. Compositional features of terrestrial planetary cores

The stability of the iron atom nucleus results in high cosmic abundance and excess iron abundances relative to other major elements like O, Si, Mg, Ca, Al and Ti, which form silicate and oxide minerals in the mantle rocks of the terrestrial (Earth-like) planets. The excess Fe segregates to form dense metallic cores. Depending on the pressures and temperatures at which metal and silicate segregate and equilibrate, additional iron-loving (siderophile) elements, especially Ni, as well as a selection of lighter elements, also enter the Fe-dominated core alloys. Figure 3 shows the density deficit and velocity excess of PREM (Dziewonski and Anderson, 1981) for the Earth's present-day molten outer core relative to molten iron (pure Fe). The observed density deficit implies that the core must contain a certain amount of one or more of the light elements Si, S, O, C, and/or H (e.g., Poirier, 1994). The exact light element composition of the outer core alloy is still controversial, with Hirose et al. (2013) listing the number of papers supporting each element ranging from ~30 for C and H, ~70 for O, ~80 for Si, and ~100 for S.

Similarly, the core compositions of the other terrestrial planetary bodies are not firmly established. Trønnes et al. (2019) summarized the probable core and mantle compositions of the terrestrial planets, and noted that a heliocentric zoning of reduced metallic Fe of the accreting material, and therefore of oxygen fugacity during core segregation, appears to be a useful guiding feature. The oxygen fugacity increased markedly from very low for the Si-rich Mercury core to very oxidized for the S-rich cores of Mars, Vesta and the iron meteorite parent bodies (Morard and Katsura, 2010; Malavergne et al., 2004, 2014; Toplis et al., 2013a, 2013b; Wood and Kiseeva, 2015; Steenstra et al., 2016; Khan et al., 2018; Steenstra and van Westrenen, 2018, 2020; Steenstra et al., 2019; Trønnes et al., 2019; Xia et al., 2019). The main indication of a strongly increasing f_{O2} during core separation is the estimated mantle FeO contents, which increase from about 0.5 to 24 wt% from Mercury to Vesta (Trønnes et al., 2019). The core mass fractions of each of the terrestrial planets, Mercury, Venus, Earth, Mars and Vesta, at increasing heliocentric distance, are negatively correlated with the FeO^{mantle} contents and oxygen fugacity. Many of the iron meteorites, demonstrating low-pressure liquid immiscibility between Fe-Ni-dominated melts (containing some P) and Fe-Ni-sulphides during their solidification, are also from parent bodies with S-rich cores, segregated under oxidizing conditions.

2.3. The Earth's core

The late stages of core segregation in the two largest terrestrial planets in our solar system, Venus and especially the Earth, occurred at very high pressures and temperatures (e.g., Laneuville et al., 2018; Lock et al., 2018; Stewart et al., 2018; Trønnes et al., 2019). The high temperatures drove the chemical exchange equilibrium: $2Fe^{metal} + SiO_2{}^{silicate} = Si^{met} + 2FeO^{sil}$ towards the product (right) side, resulting in Si-rich protocores and initial magma oceans with high FeO-contents and f_{O2} (Malavergne et al., 2004; Tsuno et al., 2013; Laneuville et al., 2018). Subsequent planetary cooling reversed the equilibrium, setting the stage for extensive chemical exchange of FeO from the magma ocean to the core and SiO_2 in the opposite direction (Trønnes et al., 2019). As shown by O'Neill et al. (1998), Tsuno et al. (2013), Hirose et al. (2017) and Helffrich et al. (2020), the combined solubility of Si and O in Fe-dominated metal at high pressures is limited, whereas the solubility of either Si or O can be very high as long as the concentration of the other element is low. Even today, the core must be strongly undersaturated with O (e.g., Takafuji et al., 2005; Frost et al., 2010), largely due to the low solid-state diffusion rates of FeO in ferropericlase and especially in bridgmanite (e.g., Holzapfel et al., 2003, 2005; Frost and McCammon, 2008).

Although the Earth's core composition is still open to debate, its physical properties, in the form of density and bulk sound velocity profiles (e.g., the PREM), are fairly well known and provide important constraints. First-principles

atomistic calculations by Badro et al. (2014), Brodholt and Badro (2017) and Umemoto and Hirose (2020) have established the density and bulk sound velocity variation as a function of concentration for the six most relevant Fe-dominated binary alloys (Figure 3). Badro et al. (2014) concluded that O is required as the main light core element, and Badro et al. (2015) favored a core with 3-5 wt% O and 2-4 wt% Si to fulfil the PREM constraints on density and velocity through the entire outer core. In addition to O and Si, the core is likely to contain minor amounts of other light elements like H, S and C.

As shown in Figure 3, an H-content of 0.5-0.8 wt% could conceivably explain the entire mismatch between the density and velocity of pure liquid Fe from the corresponding PREM values. Recently determined partition coefficients for H between metal melt and silicate melt have yielded a range of values from below unity (lithophile H) in experiments with "natural", complex silicate melts and core compositions at moderate pressures up to 20 GPa (Clesi et al., 2018; Malavergne et al., 2019) to above unity (siderophile H) for first principles thermodynamic integration in simulations with pure Fe-metal and silicate melt of $MgSiO_3$ composition up to CMB conditions (Li et al., 2020; Yuan and Steinle-Neumann, 2020). The partition coefficients, using ab initio methods might become slightly lower (closer to unity) for more complex silicate melts containing components like ferrous and ferric iron and aluminum oxides. Even with the rather high partition coefficient, $D_H^{metal/silicate}$ of about 15 at CMB conditions, derived in the Li et al. (2020) simulations, it is likely that the core contains less than about 0.1 wt% H. With a $D_H^{metal/silicate}$ of 15, a concentration of 0.1 wt% H in the core would correspond to 13 times the surface ocean inventory of H (Li et al., 2020) and a bulk mantle concentration of about 1200 ppm H_2O. The experimental determination of H partitioning at CMB conditions is extremely challenging. Although ab initio calculations are generally more straightforward, the limitations imposed by simulation cell size restrict the compositional complexity, making it difficult to model a realistic silicate melt. It is also important to avoid the "self-interaction error" related to the exchange-correlation term for the iron atoms in the simplest density functional commonly used.

Whereas near-eutectic melt fractions of sulfur-bearing metal are likely to contribute to early planetesimal cores under relatively oxidizing conditions and low to moderate pressures (Yoshino et al., 2003; Walter and Trønnes, 2004; Stewart et al., 2007; Trønnes et al., 2019), Earth accreted largely from reduced material of enstatite chondritic type. Very reducing conditions with Mercury-like core segregation are characterized by liquid immiscibility between Si-rich Fe-dominated alloy and an iron sulfide melt of composition close to FeS (Morard and Katsura, 2010; Trønnes et al., 2019). If the Earth accreted one or more Mercury-like planetary embryos, its core might have incorporated some sulfide (Wade and Wood, 2016; Wohlers and Wood, 2017; Greenwood et al., 2018). The low C/S ratios in most of the Fe-meteorite groups is likely a result of efficient silicate degassing of C on their parent bodies (Hirschmann et al., 2021). Such degassing can therefore explain extensive loss of C from terrestrial planetary bodies.

The accretion of strongly reduced sulfide-bearing materials in the form of planetesimals and planetary embryos of composition similar to that of enstatite chondrites and aubrites (Wade and Wood, 2016; Greenwood et al., 2018), probably led to incorporation of U, as well as Nd and Sm with elevated Nd/Sm ratio relative to chondrites and the bulk silicate Earth (Wohlers and Wood, 2017). Based on recent indications of very high thermal conductivity of the outer core alloy (see section 2.4), some radioactive heating of the core seems required to drive the geodynamo. It is also likely that minor amounts of other lithophile elements like Mg and Al were incorporated into the hot protocore and that their subsequent exsolution as MgO, $MgSiO_3$ and Al_2O_3 and buoyant rise into the mantle magma ocean would contribute to the earliest geodynamo (e.g., Badro et al., 2016; Trønnes et al., 2019; Helffrich et al., 2020).

2.4. Core evolution and a possible stagnant E'-layer

The enstatite chondritic nature of the Earth and high temperatures of its late-stage main core segregation and re-equilibration after the Theia collision, would likely produce an early full-grown core (proto-core) with high Si and moderate O contents, according to the displacement of the exchange equilibrium: $2Fe^{metal} + SiO_2{}^{silicate} = Si^{met} + 2FeO^{sil}$ towards the products (right side). A proto-core with relatively high Si-content, e.g., 5.1 wt% Si and 2.6 wt% O (Trønnes et al., 2019), coexisting with a FeO-rich magma ocean would be consistent with an initial non-chondritic bulk silicate Earth with low Si/(Mg+Fe) ratio. Planetary cooling would reverse the equilibrium and set the stage for extensive net chemical transport of SiO_2 from the proto-core to the magma ocean and FeO in the opposite direction. As a result of such an exchange, the protocore would evolve towards the present outer convecting core with 3.4-3.6 wt% Si and 3.0-4.0 wt% O (Badro et al., 2015; Trønnes et al., 2019). The stoichiometry of the exchange equilibrium requires the molar

FeO/SiO_2 exchange ratio to exceed 2 in order for the O-inventory of the evolving core to remain constant or increase. Although such an outer core composition, also containing about 5.5 wt% Ni, would be broadly consistent with PREM and the mineral physics data (Figure 3), minor amounts of other light elements cannot be excluded. Some of the silica transfer from the core to the magma ocean might also have occurred by exsolution of solid SiO_2 (seifertite) and $MgSiO_3$ (bridgmanite or post-bridgmanite) followed by buoyant crystals ascent (Hirose et al., 2017b; Trønnes et al., 2019; Helffrich et al., 2020)

Several studies have recognized that the seismic P-wave velocity of the outermost 200-500 km of the core decreases outwards more than PREM (Lay and Young, 1990; Garnero et al., 1993; Helffrich and Kaneshima, 2010; Kaneshima and Helffrich, 2013; Kaneshima and Matsuzawa, 2015; Kaneshima, 2018 and Irving et al., 2018). Brodholt and Badro (2017) introduced the term E' for this layer. In the seismic KHOMC model of Kaneshima and Helffrich (2013), the outward velocity deficiency relative to PREM starts from zero at 445 km depth below CMB and reaches 35 m/s (0.43%) at the CMB. Several additional studies have attempted to model the dynamics and possible stability of such a layer (e.g., Buffett, 2010; Buffett and Seagle, 2010; Gubbins and Davies, 2013). Recent experimental and ab initio theoretical determinations of the electrical and thermal conductivities of iron and several relevant outer core alloys (e.g., de Koker et al., 2012; Pozzo et al., 2012; Gomi et al., 2013; Gomi and Hirose, 2015; Ohta et al., 2016) show that they are considerably lower than those of previous geodynamo models (Stacey and Loper, 2007). These results may require additional geodynamo power from core radioactivity and early exothermic transfer of buoyant core components like SiO_2 MgO and Al_2O_3 to the magma ocean (see section 2.3). Some of these components, as well as $MgSiO_3$, may also crystallize at greater depth prior to buoyant rise, producing convective power in combination with the denser sinking liquid depleted in the light components (Badro et al., 2016; Hirose et al., 2017a; Trønnes et al., 2019; Helffrich et al., 2020). Prior to inner core growth, yielding thermal and chemical convective power at great depth, such additional sources of geodynamo power seem necessary. The onset of inner core growth is commonly estimated to be in the 1.6 - 1 Ga range (e.g., Nimmo, 2015).

The high outer core thermal conductivity supports the notion that the top of the outermost core may contain a chemically and thermally stratified layer (e.g., Pozzo et al., 2012). The existence of such a layer changes the nature of the waves and motions inside the core. Buffett (2014) has examined the consequences of the presence of the E' layer for geomagnetic fluctuations. He used the magnetic field observations at the Earth surface propagated down to the CMB and considered a generalization of the torsional oscillations in the core, the MAC waves that arise from the interplay between magnetic, Archimedes and Coriolis forces. He found that for a stably stratified core, waves with a suitable period to explain the observed fluctuations could appear. Hernlund and McNamara (2015) reviewed the merits of a stably stratified E'-layer, in spite of the very low viscosity of the core fluid. The high thermal conductivity (e.g., Pozzo et al., 2012) will generally suppress convection and the low viscosity will also reduce the viscous entrainment. A stably stratified and conducting E'-layer may even strengthen and stabilize the geodynamo which is mainly generated in the middle to lower parts of the convecting core (Sreenivasan and Gubbins, 2008; Hernlund and McNamara, 2015).

An important requirement for such a gradational layer to be stagnant over time is a reduced intrinsic density relative to the underlying convecting outer core. As expected, each of the light elements causes density deficits, but each of them also results in increased, rather than decreased, V_P, contrary to observations (Figure 3). As pointed out by Brodholt and Badro (2017), however, a partial replacement of one light element by another one, might give a suitably combined reduction in density and velocity. Because O increases the velocity and decreases the density more than Si, a partial replacement of Si by O from the outermost convecting core can yield the V_P deficit of the E'-layer. Trønnes et al. (2019) used the KHOMC deviation from PREM, combined with the mineral physics data of Brodholt and Badro (2017), to perform mass balance modelling of the E'-layer generation by transfer of SiO_2 from the outermost convecting core to the basal magma ocean and FeO in the opposite direction. The resulting E'-layer grades from 3.0 wt% O and 3.6 wt% Si and no density and velocity deficits at 445 km depth to 6.7 wt% O and 0.4 wt% Si to the required density and velocity deficits of 0.98 and 0.43%, respectively, at the CMB.

2.5. Inner core, thermal state and core dynamics

Experimental and ab initio theoretical investigations to determine the high-pressure, high-temperature phase diagram of Fe and thereby the structure of the stable solid phase of the inner core are challenging, largely due to the extreme temperature and pressure conditions. Such experiments and atomistic simulations provide melting temperature,

rheological properties, equation of state, and electrical and thermal conductivities (e.g., Hirose et al., 2013; Vocadlo, 2015; and references in Section 2.4). Laser-heated diamond cell experiments (see section 4) have reached temperatures and pressures of 5900° and 410 GPa, respectively (Tateno et al., 2012). A recent investigation of the melting curve of pure iron, using diamond anvil cell resistance heating at pressures up to 290 GPa (Sinmyo et al., 2019), resulted in a curve which is about 600 K below that of Anzellini et al. (2013), determined by laser-heating. A lower melting curve for iron at core conditions, combined with recent result indicating considerably lower solidus temperatures for peridotite at the lowermost mantle conditions (Nomura et al., 2014; Kim et al., 2020) compared to previous determinations, might possibly lead to a reduction of the average CMB temperature estimates from values of 4200-4300 K (e.g., Nimmo 2015; Vocadlo, 2015) or 4000 K (Trønnes et al., 2019) to values in the 3600-3800 K range.

Accurate knowledge of the Fe crystal structure at extreme conditions is important for estimating the physical properties such as compressibility of the inner core. In addition, it may help to understand the origin of seismic anisotropy and the dynamics in the inner core that has been proposed from the analysis of seismic waves travelling through the inner core (e.g., Souriau, 2007). In spite of some controversy, most recent studies indicate that the hexagonally close-packed (hcp) crystal structures of either pure Fe or solid alloys in the Fe-Si, Fe-C and Fe-H systems are stable at inner core conditions (e.g., Tateno et al., 2010, 2012, 2015; Stixrude, 2012; Mashino et al., 2019). In contrast, Dubrovinsky et al. (2007) and Belonoshko et al. (2017) favored the body-centered cubic (bcc) structure for Fe or an appropriate Fe-Ni alloy. Recently, Kato et al. (2020) also found that a possible FeH-dominated inner core would have face-centered cubic (fcc) crystal structure.

The thermal evolution of the Earth is driven by the decay of radiogenic isotopes and by the slow secular cooling from a temporal maximum at about 3 Ga (e.g., Herzberg et al., 2016). The thermal and compositional evolution of Earth's core is also related to the inner core growth, from a likely onset about 1.6-1.0 Gy ago (Nimmo, 2015). The outer core composition changes continuously as the inner core grows, precipitating an iron-rich alloy with a composition differing (likely more Fe-rich and possibly close to the Fe-Si join) from the evolving outer core composition. The release of latent heat of crystallization and enrichment in light elements (e.g., O) in the liquid alloy adjacent to the edge of the growing inner core e.g., have provided important thermal and compositional buoyancy, driving outer core convection and powering the geodynamo during the last 1.6-1.0 Gy.

The density jump at the present-day inner core boundary as provided by seismology (PREM model, Dziewonski and Anderson, 1981) is as large as 600 kg m^{-3}, which requires enrichment in light element(s) in the outer core relative to the inner core. This value has been recently re-evaluated and the values are ranging from 420 to 820 kg m^{-3}, recognizing the possible influence of lateral heterogeneities in the inner core and seismic noise (e.g., Hirose et al., 2013; Krasnoshchekov et al., 2019; Wong et al., 2021).

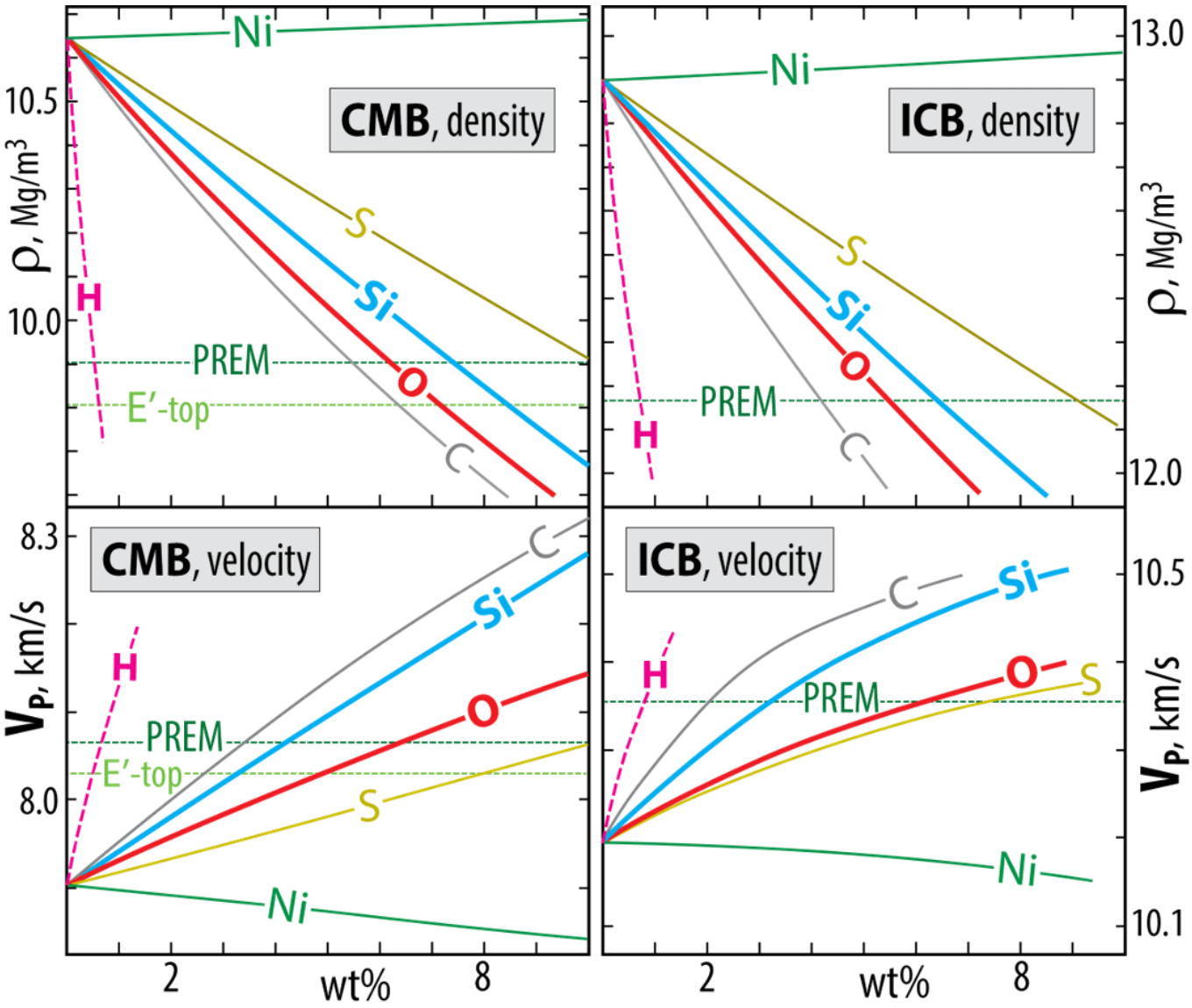

Figure 3. Density (upper panels) and velocity (lower panels) of six molten Fe-dominated binary alloys as a function of wt% of the alloying element at the approximate conditions of the core-mantle boundary (CMB, 136 GPa and 4300 K) and inner core boundary (ICB, 229 GPa and 6300 K), based on first-principles atomistic calculations. The curves for the alloys with C, S, Si and O are from Badro et al. (2014) and Brodholt and Badro (2017). The Fe-H curves are based on the Umemoto and Hirose (2020) computations, but adjusted vertically to the density and velocity of pure Fe based on Badro et al. (2014) and Brodholt and Badro (2017). The densities and velocities of PREM (Dziewonski and Anderson, 1989) and the top of the outermost E′-layer are shown by green horizontal lines. The E′-layer velocity is from the KHOMC seismic velocity model of Kaneshima and Helffrich (2013) and Kaneshima (2018) and the E′-layer density is calculated by Trønnes et al. (2019, Table 3), based on Fig. 2b of Brodholt and Badro (2017).

2.6. Geodetic constraints on the core

Finally yet importantly, it must be mentioned that the outer core viscosity is similar to that of liquid water. In addition to generating the magnetic field, the outer core undergoes a lot of external forcing from external gravitational interactions as well as from its silicate container: the mantle undergoes convection deforming the core-mantle boundary, the outer core rotates, and it changes its orientation in space.

At seasonal, interseasonal, annual, interannual, decadal, and interdecadal timescales, one sees consequences in Earth rotation changes (see Chapter Rekier et al. of this issue). One considers essentially inertial waves and rotation modes in the case of length-of-day variations and nutations and we see effects of these modes. Inertial waves, also known as inertial oscillations, are a type of wave possible in rotating fluids. The restoring force for inertial waves is the Coriolis force (Rekier et al., 2019, 2020). There are many waves that are more or less damped, and that show different repartitioning of the energy between the core and the mantle (Triana et al., 2019, 2020).

For the nutation (see Chapter Rekier et al. of this issue), this includes the effects of the Free Core Nutation (FCN) and to a minor extent the inertial waves. The FCN is a rotational normal mode that exists if one excites an angle between the rotation axes of the core and the mantle (see Figure 4).

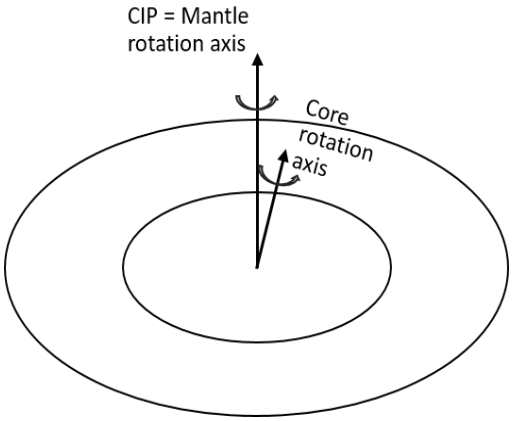

Figure 4. Geometry for the Free Core Nutation Definition.

It involves the fluid pressure acting on an ellipsoidal core-mantle boundary. One can compute a first approximation of its frequency in a frame tied to the Earth σ_{FCN} from the Liouville equations describing the angular momentum conservation equations of the global Earth and the liquid core (e.g., Sasao et al., 1980; Dehant and Mathews, 2015):

$$\sigma_{FCN} = -\Omega\left(1 + \frac{A(\alpha_f - \kappa)}{A_m}\right)$$

where Ω is the Earth angular velocity, A_m and A are the moments of inertia of the mantle and of the whole Earth respectively, α_f is the dynamical flattening of the core, and κ is the so-called compliance taking into account the deformation of the core-mantle boundary. The normal mode depends on the flattening of the core, the core deformation and the mass repartition inside the core and the mantle. One also uses the FCN frequency in inertial space σ'_{FCN}, using the link

$$\sigma = -\Omega + \sigma'$$

between the inertial space frequency σ' and the frequency in a frame tied to the Earth σ:

$$\sigma'_{FCN} = \Omega + \sigma_{FCN} = -\Omega\left(\frac{A(\alpha_f - \kappa)}{A_m}\right) \quad (4)$$

The FCN induces resonances in the nutation amplitudes. The nutation amplitude $\eta(\sigma')$ at frequency σ' can be computed from the rigid-Earth nutation $\eta_{rigid}(\sigma')$ and the transfer function $TF(\sigma)$.

$$\eta(\sigma') = TF(\sigma)\,\eta_{rigid}(\sigma')$$

The transfer function is function of the FCN frequency

$$TF(\sigma \text{ or } \sigma') = \frac{-kA}{A_m} - \frac{(1+k)A}{A_m(\sigma - \sigma_{CW})} + \frac{A_f \sigma'_{FCN}}{A_m(\sigma' - \sigma'_{FCN})} \cong \frac{A}{A_m} + \frac{A_f \sigma'_{FCN}}{A_m(\sigma' - \sigma'_{FCN})}$$

in the retrograde diurnal approximation in a frame tied to the Earth, where k is the tidal Love number for the mass repartition induced by deformation and σ_{CW} is the Chandler Wobble frequency, and where we see that the transfer function for nutations contains a resonance at the FCN frequency.

There is, in addition, an excitation of the free mode, which could also help constrain core properties (Zhu et al., 2020). Figure 5 show the evolution of the free mode excitation as observed in the VLBI data over the past three decades.

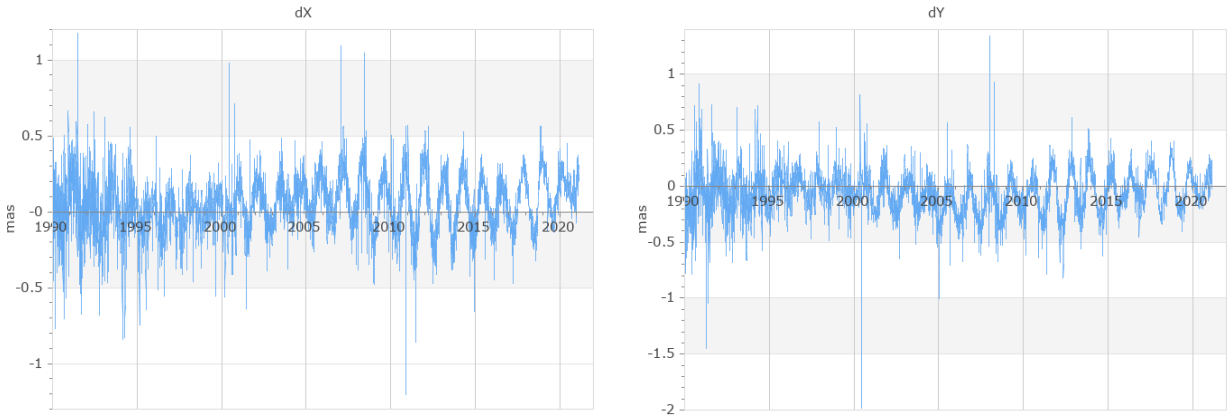

Figure 5. Residuals (given in milliarcsecond (mas) as a function of time) of the CIP (Celestial Intermediate Pole) position (dX and dY) between the observed nutation (observed by Very Long Baseline Interferometry, VLBI) and the most accurate model that exists at present, over the past three decades. This figure has been built from the IERS – Observatoire de Paris website [https://hpiers.obspm.fr/eop-pc/index.php?index=orientation&lang=en], for the years 1990-2021. See also Rekier et al. (this issue).

Together with Earth rotation changes (see Chapter Rekier et al. of this issue), the nutations can provide additional geodetic information about core properties and processes such as the coupling mechanisms acting at the core-mantle boundary and at the inner core boundary. Details are provided in Rekier et al. (Chapter of this issue).

3. Core-mantle boundary

The properties of the core-mantle boundary (CMB) region can be obtained mostly from seismology, based on either compressional (P) or shear (S) wave travel times (e.g., Morelli and Dziewonski, 1987). Seismic phases that have been used for this purpose (e.g., Koelemeijer et al., 2016, 2017) include PKP (compressional waves travelling through the outer core) and PKIKP (compressional waves travelling through both the outer and inner core). Other approaches include studying seismic eigenmodes splitting (e.g., Li et al., 1991; Ishii and Tromp, 2001) and seismic waves that reflect at the metal-rock interface in the CMB ((ScS, PcP seismic phases, e.g., Boschi and Dziewonski, 1999; Vasco et al., 1999; Soldati et al., 2003; Boschi et al., 2013).

Recently, mantle normal mode observations have been shown to be very useful to constrain properties and processes of the CMB as well. In order to constrain the density and viscosity of the mantle close to the CMB, one can use normal modes that are particularly sensitive to their variations, called Stoneley modes ${}_2S_{16}$ and ${}_3S_{36}$ (Koelemeijer et al., 2017). The predicted effects of the presence of LLSVPs with varying density excesses compared to the surrounding lower mantle can be compared with observations. Using this approach, Koelemeijer et al. (2017) showed that relatively low excess densities of LLSVPs are more probable, which according to the authors, would explain the excess of ellipticity and the zones of ascent above the LLVPs (see Figure 1).

In parallel, the CMB topography, and its flattening in particular, has been constrained from geodetic data, i.e. from length-of-day variations (e.g., Hide and Horai, 1968; Jault and Le Mouël, 1990) as well as from the nutations (e.g., Gwinn et al., 1986; Mathews et al., 2002). The latter are sensitive to the core-mantle boundary flattening and coupling mechanisms (see Rekier et al., this issue). Geomagnetic field data analysis can also provide important ancillary clues on the CMB location and its topography (e.g., Glatzmaier and Roberts, 1996; De Santis and Barraclough, 1997), although the associated resolution is much lower than that provided by seismological studies.

CMB topography can also be obtained from dynamical considerations, considering that the mantle contains density anomalies as seen from the seismic tomography, and computing the associated loading on the CMB. The CMB topography mainly shows long-wavelength features related to the subduction of plates deep into the mantle and as actively upwelling material rising in deeply rooted hotspots or, in the upper mantle, as passively upwelling material underneath mid-ocean ridges. Numerical studies have shown that these long-wavelength features are mainly driven by the mass anomalies at the bottom of the mantle, with the CMB topography responding similar to isostasy. The numerical dynamic studies have also shown that the amplitudes of these topographic variations depend on the viscosity at the bottom of the mantle (e.g., Defraigne et al., 1996; Dehant and Wahr, 1991). Numerical modelling of

mantle flow and the induced dynamic CMB topography aids in the interpretation of these observational constraints (e.g., Forte et al., 1995; Forte and Mitrovica, 2001; Forte, 2007; Yoshida, 2008; Steinberger and Holme, 2008; Simmons et al., 2009; Lassak et al., 2010; Soldati et al., 2012, 2013; Liu and Zhong, 2015; Deschamps et al., 2018). Some of these studies show significant differences in model outcomes (e.g., Soldati et al., 2012) and some suggest that all available data should be inverted together to better constrain the CMB topography (e.g., Colombi et al., 2014; Simmons et al., 2010). These authors had the idea to resolve the 3D image of the mantle and CMB, by combining multiple data types. They use the predicted velocity structure from the model where the seismic constraints are weak, filling in the gaps. The model so obtained, termed GyPSuM (G = Geodynamic, y, P = P waves, S = S waves, u, M = Mineral physics), provides mantle wave speeds and densities. One sees in the literature several approaches, either considering thermal models for the interpretation of the densities at the bottom of the mantle or thermo-chemical models.

Inferences for the CMB that can be derived from the above-mentioned studies are the following:

- For density in the bottom of the mantle, average models consistently identify two areas of dense anomalies; one located below Southern Africa (centered on Angola), roughly in the core of the LLSVP imaged in seismic velocity. The other one is found under the North Pacific (close to Hawaii), located more on the edge of the LLSVP as imaged in seismic velocity (see Figure 1).
- Seismic observations, Stoneley modes (Koelemeijer et al., 2017) and tidal measurements (Lau et al., 2017) show similar features, summarized in the paragraphs on the mantle of this chapter. There we show that, to unravel the nature of the lower mantle features, knowledge of more than one elastic parameter is needed, i.e. constraints on V_P are required in addition to V_S. All data point to the conclusion that LLSVPs must be chemically. Although unique interpretations are difficult, a comparison with recent work by Deschamps et al. (2018) suggests that strongly thermochemical models are inconsistent with current seismological models.
- There is no convergence towards a global model of the bottom mantle anomalies to derive a topographic map of the CMB unambiguously. One of the avenues for finding constraints or getting a better precision close to the CMB is the use of the normal modes called the Stoneley modes. However, their digital implementations remain complicated. These models are thus often restricted to using an initial model that does not include any lateral heterogeneity (model of PREM), which explains the under-representations of the models of normal modes.
- Topography models mostly show elevated topographies under the Pacific and Africa, but details differ between models. Almost all models have a peak-to-peak amplitude below 5 km for degree 2.

It is thus important to develop models based on an increase of the variety of data and of the amount of data on which to base an interpretation. It is interesting to develop models not only based on propagation speeds of seismic waves or reflected and refracted seismic waves, but as well on normal modes, on geodetic data and on the use of gravimetry to detect mass anomalies present in the mantle. At this point, it is still crucial to develop robust models of CMB topography that are compatible with such a large range of data.

Understanding what is going on at the CMB is crucial as well. As detailed in Rekier et al. (Chapter of this issue), there are different coupling mechanisms between the core and the mantle: the topographic torque (or pressure torque) related to the pressure acting on a bumpy boundary (e.g., Hide, 1977), the gravitational torque, the viscous torque, and the electromagnetic torque. In terms of processes that could take place at the CMB, one may consider the existence of percolation (Mandea et al., 2015).

4. High-pressure experiments to constrain core and mantle properties

Quantitative interpretation of geochemical, seismological, and geodetic observations related to the deep Earth requires experimental measurements of the high-pressure and high-temperature physical and chemical properties of silicate and metal solid phases as well as silicate and metal melts. Some of these experiments, particularly those dealing with measurements of the equilibrium major and trace element composition of co-existing phases, can be performed in high-pressure laboratories situated on university campuses or research institutes. Such experiments require achieving stable, hydrostatic pressure conditions for the duration of the experiment (which typically lasts between minutes and 24 hours depending on the temperatures involved). These experiments are ended by rapidly (typically in 10-30 seconds) lowering sample temperatures from >1000 K to <325 K, “freezing in” chemical compositions that were set at the high temperature of the experiment. Such experiments are typically followed by analyses using state-of-the-art microbeam techniques, enabling detailed chemical compositional measurements of the run products.

Other experiments, especially those related to physical property measurements, require so-called *in situ* techniques, probing sample properties while the sample is experiencing high pressure and/or high temperature conditions. These experiments are typically performed using a range of synchrotron X-ray diffraction and absorption, neutron-based techniques. Facilities that combine high-pressure equipments capable of generating static high pressures used by deep Earth scientists with these analytical capabilities are at present only available at large-scale facilities, including around a dozen major centers in the US (e.g., APS and NSLS), Europe (e.g., ESRF in France, PETRA-III at DESY in Germany, Diamond in the UK, and PSI in Switzerland), Japan (e.g., SPring-8 and the Photon Factory), and China (e.g., SSRF). Experiments in which sample pressures are not static but dynamic (creating transient high-pressure states by for example hitting a sample with a high-velocity projectile, or irradiating a sample with a high-intensity laser pulse) also generally require the use of large-scale joint facilities, although a small number of university-based facilities exist.

High-pressure, high-temperature experiments are also increasingly performed *in silico*, using first principles molecular dynamics simulations. Major advantages of these include that they can uniquely provide an atom-scale view of processes and properties, and that they can reach pressures and temperatures out of reach of experimental equipment. A disadvantage is that simulating multi-component systems representing lower mantle or core compositions can still be prohibitively expensive computationally (leading to many simulation studies focusing, for example, on end member compositions such as pure $MgSiO_3$ for bridgmanite). Another issue is that although these *in silico* approaches provide accurate information on relative changes in properties under changing conditions (for example, the calculated change in density of a mineral as a function of pressure compared to the calculated density at ambient pressure and temperature (ρ/ρ_0), the agreement with absolute property measurements using traditional experimental approaches (for example, the absolute value calculated for ρ_0 compared to the experimentally determined value of ρ_0) can remain suboptimal.

In this section, the main experimental high-pressure equipment currently used to study the chemical and physical properties of Earth materials at high pressure and high temperature is briefly reviewed. Readers interested in the history of high-pressure science are referred to Hazen (1999). This review will focus on static compression techniques, and will not discuss dynamic compression or *in silico* techniques. Dynamic compression experimental as well as analytical techniques are reviewed in McMahon (2020).

Crustal and upper mantle pressures between ~0.5 and ~5 GPa (with most setups capable of a maximum of ~3 GPa) at temperatures of up to approximately 1873 K can be reached with a single stage piston cylinder press (Boyd and England, 1960). In such a press a cylindrical assembly, typically 10-25 mm in diameter, is used (an example is given in Figure 6a). The sample is chemically isolated from its exterior through the use of a noble metal capsule, which is surrounded by high-temperature ceramic materials, a cylindrical graphite heater, and insulating materials, which, depending on the temperatures required, can consist of cylinders of NaCl, barium carbonate, or talc combined with silica glass or pyrex (e.g., McDade et al., 2002). The assembly is inserted into the center of a pressure plate consisting of an inner high-strength tungsten carbide (WC) core and an outer softer steel shell. The sample is then compressed by a WC piston and heated through resistive heating of the graphite furnace. Typical sample volumes are on the order of 5-60 mm^3.

Piston cylinder presses are not suitable for *in situ* experimentation because the samples are completely surrounded by metal parts preventing access of probing radiation. Some indirect measurements of physical properties of earth materials are nevertheless possible. For example, the so-called falling sphere technique can be used to determine the density of silicate magma relative to the density of minerals at high pressures and high temperatures. This can be achieved by loading spherical mineral grains at the top and bottom of a powdered glass sample, and checking after a piston cylinder experiment whether the mineral grains have sunk, floated, or remained in their original positions (pointing to neutral buoyancy). Using equations of state of minerals these experiments can be used to constrain the density of magma in piston cylinder press experiments (e.g., Agee, 1998; Van Kan Parker et al., 2011a).

Upper mantle and transition zone pressures (from ~3 to approximately ~23 GPa, equivalent to 660 km depth) can be achieved in so-called Large Volume Presses (LVP), often using a two-stage multi-anvil technique (e.g., Kawai and Endo, 1970; Walker et al., 1990). Although a range of different multi-anvil presses have been designed and built, most high-pressure assemblies used in these apparati are octahedral in shape (e.g., Figure 6b), with dimensions depending on the desired sample pressure. In the most common type of multi-anvil, the Kawai-type or 6-8 type, the octahedra are

compressed via the corners of eight cube-shaped second-stage anvils that are traditionally made from tungsten carbide. The corners of the cubes that touch the sides of the octahedra are truncated, with smaller truncations enabling higher sample pressures. The set of eight second-stage cubes is backed by six first-stage steel anvils. Samples can be subjected to high pressure when a hydraulic ram progressively decreases the distance between the second-stage anvils by moving the fist-stage anvils. Using resistive heating of graphite (at low pressure), lanthanum chromite or rhenium (at high pressure), stable sample temperatures exceeding 2500 K can be achieved. Sample volumes in these LVP devices are on the order of 1 mm^3 (with some very large presses able to process significantly larger volumes particularly suitable for high-quality sample synthesis), sufficient for studies of the partitioning of major and minor elements between silicate minerals and silicate melts in the mantle (important, for example, for magma ocean solidification studies); of the phase relations and evolving mineral compositions in various bulk compositions thought to be present in Earth's mantle, of the partitioning of elements between silicate melt and metal melt (key to models of initial core-mantle segregation in the Earth and subsequent core-mantle chemical interaction); and of diffusion rates in minerals and magmas at high pressure (Ito and Takahashi, 1989).

The open space between the eight second-stage anvils, combined with the possibility of widening gaps between the outer anvils by adjusting their shapes, makes it possible for multi-anvil apparatus to be used for *in situ* experiments. Phase transitions in Earth's upper mantle and transition zone, the mineralogy of the top of Earth's lower mantle, and key physical properties such as mineral densities, P and S wave propagation velocities, deep magma viscosities, and reaction rates can be studied *in situ* with a multi-anvil.

Lower mantle studies are becoming increasingly feasible with multi-anvil devices. With the classic Kawai-type 6-8 design and WC second-stage anvils, maximum pressures were close to 26 GPa due to the limitations of the strength of the WC cubes in combination with the uniaxial nature of the overall compression in the press. This meant only the very top of the lower mantle could be studied with this equipment. In recent years, by increasing the freedom with which the first-stage anvils can move and rotate during compression, or by replacing a hydraulic ram to move the first stage anvils by an oil bath pressing onto the outside of the first stage anvils directly (Ito and Takahashi, 1989; Stewart et al., 2007) stresses in WC cubes have been limited, and pressures between 27 and over 40 GPa have been achieved (e.g., Ishii et al., 2016). In addition, tungsten carbide cubes can be replaced by sintered diamond cubes, enabling *in situ* property measurements at pressures of >100 GPa in multi-anvil devices (e.g., Yamazaki et al., 2014).

Although these developments indicate that multi-anvil techniques are starting to approach the pressure-temperature field of direct relevant to Earth's core-mantle boundary region and core, most experimental studies aiming to obtain in particular physical property measurements of materials in these deepest regions in the Earth require the use of diamond anvil cells (DACs). With the DAC technique, developed in parallel by two groups in the 1950s (Jamieson et al., 1959; Weir et al., 1959) very small samples (with diameters on the 10s to 100s micrometer scale) are compressed between the opposed tips of two single-crystal diamonds (Figure 6c). The DAC can be used at pressures overlapping with those of the piston cylinder and multi-anvil apparati discussed above, but can also be used to achieve pressures exceeding those in the center of the Earth. Resistive heating is used in some DAC applications that mostly focus on relatively low temperature applications, but in most cases DAC is combined with laser heating (achieved by sending laser beams through one or both diamonds and achieving high temperatures by the laser light coupling to the sample material). Sample temperatures cannot be measured by thermocouples anymore, and instead the radiative spectrum of light emitted by the sample is used to constrain temperatures (e.g., Mao and Hemley, 1998; Mao et al., 2018).

The DAC setup provides unique access to the samples while they experience high pressure, high temperature conditions due to the transparency of the diamonds, enabling a wide range of *in situ* techniques to be applied (McMahon, 2020). Although most measurements in a DAC consider physical properties, technical developments including improved capabilities to provide a stable and flat temperature profile across a large part of a sample increasingly enable studies of chemical properties such as melting behavior at lower mantle conditions (e.g., Tateno et al., 2010; Andrault et al., 2018) or in the core (e.g., Miozzi et al., 2020). Figure 7 summarizes the approximate current capabilities of the static high-pressure devices described above in comparison to conditions in the Earth. One final note to make is that the precision of temperature measurements at the conditions of the deep Earth is improving, but that increasing the accuracy of extreme temperature measurements remains very challenging. As a result, error bars on temperature measurements in diamond anvil cell experiments can easily be several 100 degrees.

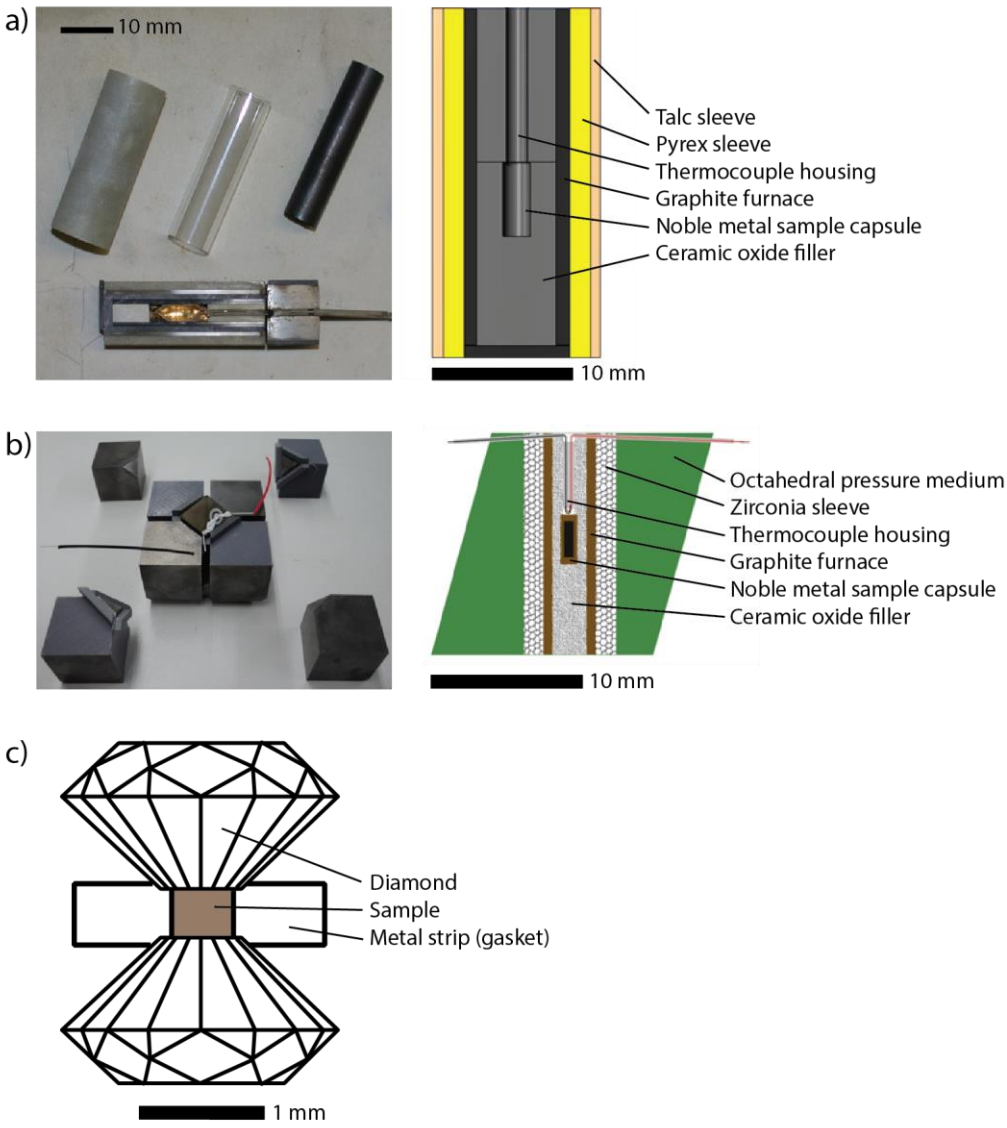

Figure 6. Examples of static high-pressure experimental setups. (a) Talc-pyrex piston cylinder assembly (as described in Van Kan Parker et al., 2011b), with sample parts on the left and cross-section drawing on the right (b) Typical octahedral multi-anvil assembly, with picture of a set of eight second-stage tungsten carbide cubes containing an octahedral pressure medium on the left, and a cross-section drawing on the right (from Knibbe et al., 2018) (c) Diamond anvil cell cross-section.

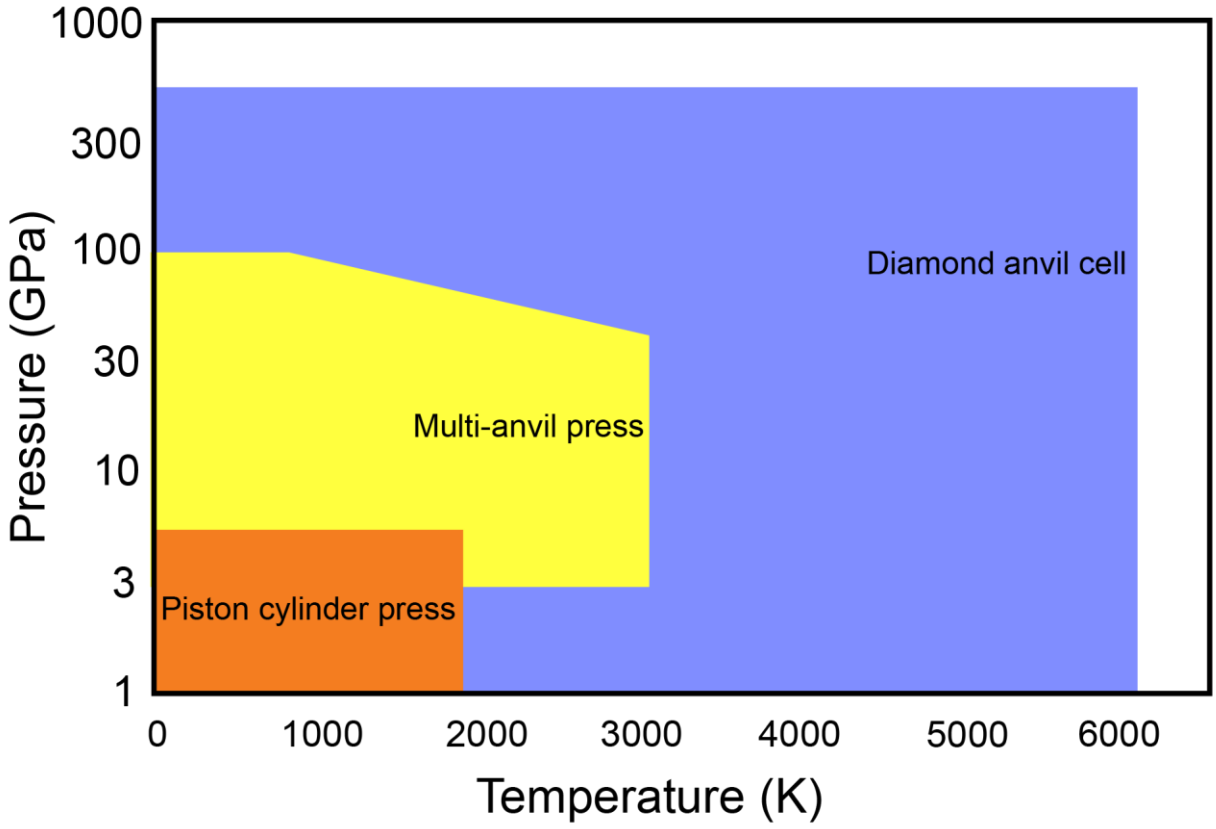

Figure 7. Compilation of current approximate pressure-temperature capabilities of static high-pressure, high-temperature experimental equipment.

5. Magnetic field enlightening the core

Earth's magnetic field is generated in the liquid outer core. Changing flow patterns of the molten metal present in the outer core provide the variability of the geomagnetic field, both at very long (million to billion year) time scales and at short time scales (e.g., Olsen and Mandea, 2008). The theory of liquid convection in fast rotating planetary spherical shells is behind these variations, as discussed also in Le Bars et al. (this issue). For a fluid shell with a positive temperature gradient imposed between inner and outer core boundary, convection starts as columns outside the tangent cylinder (i.e. Inner Core Boundary, ICB) parallel to the Earth rotation axis (see Fig. 1 in Duka et al., 2015). Motion in form of a vortex around the axis of the column produces cyclonic and anticyclonic columns rotating in the same and in the opposite direction, respectively (Busse, 1975). Secondary flows are directed away from the equatorial plane in anticyclonic columns, and in cyclonic columns towards the equatorial plane.

It is not possible to measure the geomagnetic field directly at outer core depths, so understanding better how these processes work is only possible through magnetic measurements at surface or satellite heights. The inversion of the three-component observations (X-North, Y-East, Z-towards Center) of the geomagnetic field is usually performed in Spherical Harmonic Analysis of the potential field in terms of Gauss coefficients and then, taking advantage of the Laplacian properties of the field, can be projected downward to the top of the outer core, supposing an insulating mantle without magnetic sources. Although the latter hypothesis is not perfect, it works for inferring most of the static and dynamic properties of the core (e.g., Backus et al., 1996). This approach gives rise to the so-called geomagnetic field models or reconstructions. Another way to address the problem is using numerical modelling of core dynamics based on the magneto-hydrodynamical equations for convection and magnetic field generation by taking advantage of the information contained in these geomagnetic field models and new approaches based on the data assimilation techniques (for a review about geodynamo modelling see Wicht and Sanchez, 2019).

At the Earth's surface, the dipole component of the geomagnetic field accounts for more than 90% of the entire geomagnetic field. From the first direct measurements of the geomagnetic field intensity in 1840, a decreasing of around 9% of the dipole moment of the Earth's magnetic field has been observed. This decay has experienced an acceleration from 1990 (Thébault et al., 2015) and it seems to coincide with the presence of one of the most intriguing

features of the present-day geomagnetic field, i.e. the South Atlantic Anomaly (SAA). This anomaly covers part of South America, the southern Atlantic Ocean and Africa and is related to lower values of the surface intensity than expected in the area. From 1840, it is observed that the SAA areal extent is continuously growing with periods of accelerations and decelerations (Pavón-Carrasco and De Santis, 2016).

The SAA is linked with the presence of Reversed Flux Patches (RFPs) at the Core-Mantle Boundary (CMB) (e.g., Terra-Nova et al., 2017) (Figure 8). It has been observed that these patches are located beneath South Africa and South America and in the last years, the South African RFP has been reinforcing (e.g., Pavón-Carrasco and De Santis, 2016). This situation has been recently reflected at the surface with a split in two different cells of the SAA, one of them over South America and a new one located in the South Atlantic Ocean very close to South Africa (https://www.esa.int/Applications/Observing_the_Earth/Swarm/Swarm_probes_weakening_of_Earth_s_magnetic_field).

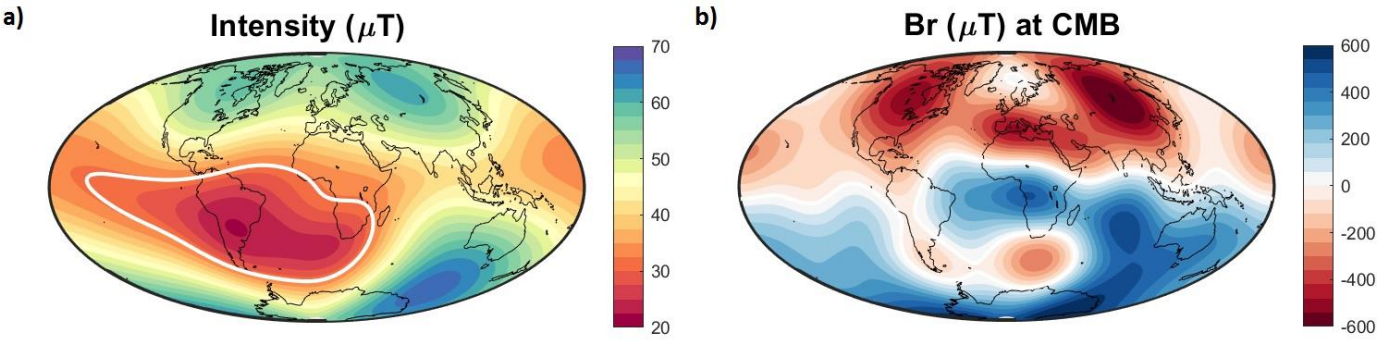

Figure 8. Geomagnetic field on January 1, 2020. (a) Intensity at the surface and (b) radial component (Br) of the geomagnetic field at the CMB on January 1, 2020, from CHAOS-7.2 model (Finlay et al., 2020). The white line in (a) marks the contour line of 32,000 nT to highlight the area of the SAA defined following De Santis et al. (2012). In (b) the two RFPs related to the presence of the SAA at the surface are observed in red colors in the Southern Hemisphere. CHAOS-7.2 model is used until degree 13 to calculate the intensity at the surface and until degree six for Br at the CMB. From Campuzano et al. (2021).

The current decay of the dipole moment and the presence of the SAA related to RFPs at the CMB has motivated some authors to think about a possible upcoming geomagnetic transition, such as an excursion or a reversal (De Santis et al., 2013; Laj and Kissel, 2015; Pavón-Carrasco and De Santis, 2016). Considering the geomagnetic field as a critical system following De Santis et al. (2013) and De Santis and Qamili (2015), one can estimate a critical time when a possible transition would occur by modelling the recent behavior in time of SAA with a log-periodic singular function. If this behavior is maintained in time, this will provide a critical time of non-return point for a transition around 2030-2060 AD. However, the uncertainty is large, and more data are needed (at least one or two decades more) to better validate this model. It is worth noting that the present value of the dipole moment is not comparable with values previously associated with geomagnetic transitions recorded in rocks (see e.g., Pavón-Carrasco et al., 2014). On the other hand, the current rate of decay is comparable with that observed during previous reversals (Laj and Kissel, 2015). Another way to approach the study of reversals is to use numerical models to better understand the physical processes involved in polarity transitions. One of the first attempts with a numerical geodynamo model was carried out by Glatzmaier and Roberts (1995), but simpler approaches can be also explored. An example of this could be found in the work of Duka et al. (2015). These authors considered a “domino” model to study geomagnetic field reversals. This simplified model consists of a ring of interacting magnetic macrospins placed close to the ICB. Duka et al. (2015) found a good agreement between the secular variation of the dipolar geomagnetic field by previously published models and those given by the “domino” model as well as good approaches to a long series with polarity reversals. The work also showed a reversal about 75,000 years from now, but it is important to note that this cannot be considered as the exact prediction of a reversal, rather as a probable behavior of the dipolar geomagnetic field in the near future.

Another peculiar feature of the current geomagnetic field is the rapid movement of the north magnetic pole with respect to the geographic South Pole, moving from the Canadian Arctic towards Siberia, reaching a present-day velocity of 50-60 km per year (Livermore et al., 2020). Magnetic poles are defined as the points where the inclination of the geomagnetic field is equal to ±90º. The recent acceleration of the north magnetic pole observed over the last decades

can be explained by the balance between two large lobes of negative flux at the CMB (i.e. Normal Flux Patches, NFPs), here in particular under the regions of Canada and Siberia.

Intriguing relations have also been found between the geomagnetic field and climate in the past at different temporal and spatial scales (e.g., Gallet et al., 2005; Courtillot et al., 2007; Usoskin et al., 2008). One of the most recently published works regarding this topic is linked with the evolution of the SAA over the last 300 years (Campuzano et al., 2018). In this case, the connection is established with transfer entropy, a tool used in non-linear dynamic studies (Schreiber, 2000). This parameter is able to provide information about the existence of a link between two time series and the direction in which this link is produced. The results provided by Campuzano et al. (2018) are based on a previous study that observed a long-term relation between the SAA areal extent and Global Sea Level (GSL) rise for the last three centuries (De Santis et al., 2012). The transfer entropy provided with about 90% of confidence that the short-term link between these two variables exists and goes from SAA (representing geomagnetic field system) to GSL (climate system). This work is interesting because it could help in the determination of a successful physical mechanism able to explain this connection. One of the hypotheses could be an internal mechanism by which a convective dynamism in the outer core could cause a variation of the magnetic field and an elastic deformation at the Earth's surface (Greff-Lefftz et al., 2004).

A recent finding regarding the SAA evolution is the possible relation between the occurrence of geomagnetic jerks and the SAA areal extent (Campuzano et al., 2021). Geomagnetic jerks are abrupt and sharp changes in the secular variation of the geomagnetic field (Figure 9a) especially well-observed in the East component of the geomagnetic field recorded in magnetic observatories. It seems that jerks occurring during the last two decades happen very close to the minima of the SAA areal extent acceleration (Figure 9b). This implies some kind of mechanism that could relate both phenomena and its internal origin. In 2019, Kloss and Finlay (2019) provided evidence for the possible interior origin of the geomagnetic jerks and later Aubert and Finlay (2019) used a magneto-hydrodynamics model and showed that jerks could be produced by the arrival of localized Alfven wave packets radiated from sudden buoyancy releases inside the core. These waves would reach the core surface and focus their energy towards the equatorial plane and along lines of strong magnetic field, creating sharp inter-annual changes in the core flow.

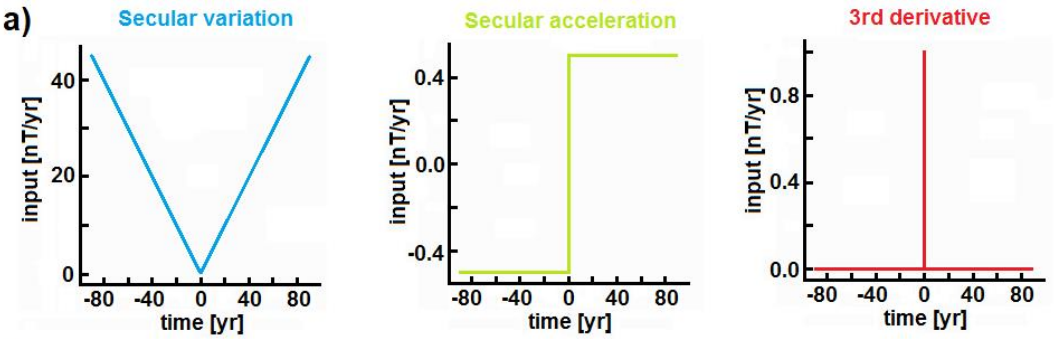

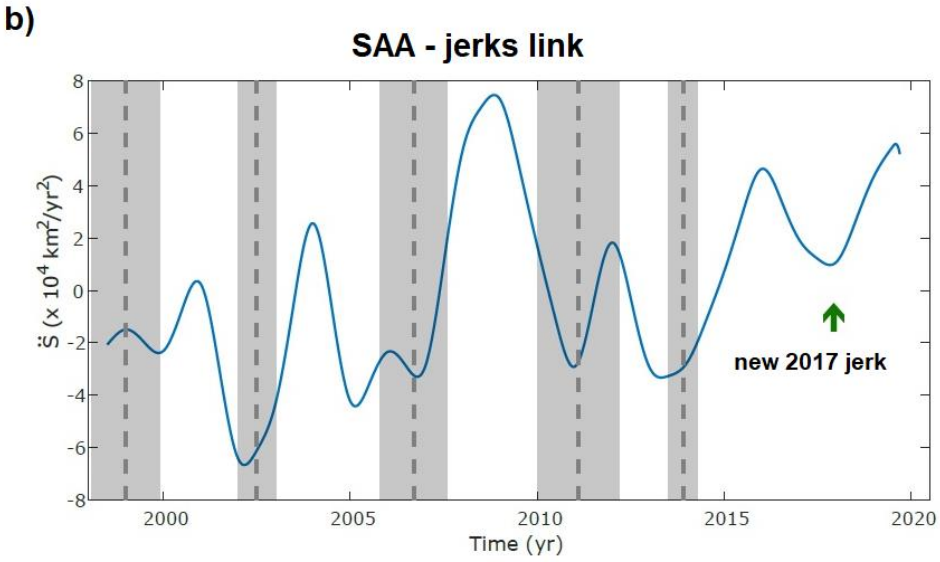

Figure 9. a) Schematic representation of secular variation for a hypothetical component of the magnetic field. The first graph shows the typical V-shape of jerks in the secular variation and the second and third show the secular acceleration and the third differences, respectively. b) Second derivative S̈ (i.e. acceleration) of the areal extent of the SAA for the last 2 decades calculated from CHAOS-7.2 model monthly from January 1998 to March 2020. In dashed vertical gray lines, the mean occurrence times of the well-defined geomagnetic jerks for the last 2 decades are marked. Shaded bands mark the uncertainty of the occurrence times given by one standard deviation. The green arrow indicates the presence of a new jerk in 2017. From Pinheiro and Travassos (2010) and Campuzano et al. (2021).

Another intriguing characteristic of the present geomagnetic field is its chaotic and turbulent dynamics. These features cannot be seen directly but is found in the analyses of geomagnetic observatory time-series (Barraclough and De Santis, 1997; De Santis et al., 2003). De Santis and Barraclough (1997), from the decay of the geomagnetic field spatial power spectrum as shown by global models of the last 400 years, speculated that the CMB is fractal with a fractal dimension 1.2, as evidence of a turbulent but organized outer core, as further supported by the inter-relation between temporal and spatial power spectra of the geomagnetic field (De Santis et al., 2003).

From this brief overview, it is clear that studying key features and short-term variations in the geomagnetic field can help better understand he processes taking place in the core. What developments can we expect in the future? Will it be possible to predict ahead of time an impending geomagnetic jerk? What about the timing of an eventual future geomagnetic transition or link with climate change? Taking advantage of the properties of the geomagnetic field being chaotic and ergodic (De Santis et al., 2011), one can show that (1) it can be characterized by a mean exponential time scale after which it is no longer predictable and (2) time analyses can replace the more difficult phase space analyses. Addressing the first question and considering that the capability to predict the geomagnetic field decreases during geomagnetic jerks, Qamili et al. (2013) proposed a method to detect these events, confirming the most well known jerks and suggesting others.

However, the definitive answer to these questions is not clear. Maybe the clues for the future will be in (1) the acquisition of more magnetic data coming from both the past (remanent magnetization of sedimentary rocks or archeological artifacts and lava flows) and the present (satellites, magnetic observatories at ground) and (2) the implementation of new powerful techniques such as machine learning or artificial intelligence.

References

Agee, C.B., 2008, Static compression of hydrous silicate melt and the effect of water on planetary differentiation. Earth Planet. Sci. Lett., 265, 641-654.

Amman, M.W., Brodholt J.P., Wookey J., and Dobson D.P., 2010, First principles constraints on diffusion in lower-mantle minerals and a weak D" layer. Nature, 465, 462-465, DOI: 10.1038/nature09052.

Andersen, M., Elliott T., Freymuth H., Sims K.W.W., Niu Y., and Kelley K.A., 2015, The terrestrial uranium isotope cycle. Nature, 517, 356-359, DOI: 10.1038/nature14062.

Andrault, D., Pesce G., Bouhifd M.A., Bolfan-Casanova N., Hénot J.M., and Mezouar M., 2014, Melting of subducted basalt at the core-mantle boundary. Science, 344(6186), 892-895, DOI: 10.1126/science.1250466.

Andrault, D., Pesce G., Manthilake G., Monteux J., Bolfan-Casanova N., Chantel J., Novella D., Guignot N., King A., Itié J.P., and Hennet L., 2018, Deep and persistent melt layer in the Archaean mantle. Nature Geoscience, DOI: 10.1038/s41561-017-0053-9.

Anzellini, S., Dewaele A., Mezouar M., Loubeyre P., and Morard G., 2013, Melting of iron at Earth's inner core boundary based on fast X-ray diffraction. Science, 340, 464-466.

Aubert, J., and Finlay C.C., 2019, Geomagnetic jerks and rapid hydromagnetic waves focusing at Earth's core surface, Nat. Geosci., 12, 393-398, DOI: 10.1038/s41561-019-0355-1.

Backus, G., Parker R., and Constable C., 1996, Foundations of Geomagnetism, Cambridge Univ. Press.

Badro, J., Côté A.S., and Brodholt J.P., 2014, A seismologically consistent compositional model of Earth's core. Proceedings of the National Academy of Sciences, 111(21), 7542-7545, DOI: 10.1073/pnas.1316708111.

Badro, J., Brodholt J.P., Piet H., Siebert J., and Ryerson F.J., 2015, Core formation and core composition from coupled geochemical and geophysical constraints. Proceedings of the National Academy of Sciences, 112(40), 12310-12314, DOI: 10.1073/pnas.1505672112.

Badro, J., Siebert, J., and Nimmo, F., 2016, An early geodynamo driven by exsolution of mantle components from Earth's core. Nature, 536, 326-328.

Ballmer, M.D., Schmerr N.C., Nakagawa T., and Ritsema J., 2015, Compositional mantle layering revealed by slab stagnation at 1000-km depth. Science Advances, 1(11), Id. e1500815, DOI: 10.1126/sciadv.1500815.

Ballmer, M.D., Schumacher L., Lekic V., Thomas C., and Ito G., 2016, Compositional layering within the large low shear-wave velocity provinces in the lower mantle. Geochemistry, Geophysics, Geosystems, 17(12), 5056-5077, DOI: 10.1002/2016GC006605.

Ballmer, M.D., Houser C., Hernlund J., Wentzcovitch R.M., and Hirose K., 2017, Persistence of strong silica-enriched domains in the Earth's lower mantle. Nature Geoscience, 10, 236-240, DOI: 10.1038/ngeo2898.

Baron, M.A., Lord O.T., Myhill R., Thomson A.R., Wang W., Trønnes R.G., and Walter M.J., 2017, Experimental constraints on melting temperatures in the MgO-SiO_2 system at lower mantle pressures. Earth and Planetary Science Letters, 472, 186-196, DOI: 10.1016/j.epsl.2017.05.020.

Barraclough, D.R., and De Santis A., 1997, Some possible evidence for a chaotic geomagnetic field from observational data. Phys. Earth Plan. Inter., 99, 207-220.

Bauer, A.M., Reimink J.R., Chacko T., Foley B.J., Shirey S.B., and Pearson D.G., 2020, Hafnium isotopes in zircons document the gradual onset of mobile-lid tectonics. Geophys Perspect Lett, 14, 1-6, DOI: 10.7185/geochemlet.2015.

Becker, T.W., and Boschi L., 2002, A comparison of tomographic and geodynamic mantle models, Geochem. Geophys. Geosyst., 3, 1003, DOI: 10.1029/2001GC000168.

Belonoshko, A.B., Lukinov T., Fu J., Zhao J., Davis S., and Simak S.I., 2017, Stabilization of body-centred cubic iron under inner-core conditions. Nature Geoscience, 10, 312-316.

Boschi, L., and Dziewonski A., 1999, High and low resolution images of the earth's mantle – implications of different approaches to tomographic modeling, J. Geophys. Res., 104, 567-594.

Boschi, L., Weemstra C., Verbeke J., Ekstrom G., Zunino A., and Giardini D., 2013, On measuring surface-wave phase velocity from station-station cross-correlation of ambient signal. Geophys. J. Int., 192, 346-358.

Boyd, F.R., and England J.L., 1960, Apparatus for phase-equilibrium measurements at pressures up to 50 kilobars and temperatures up to 1750°C. Journal of Geophysical Research, 65, 741-748.

Brodholt, J., and Badro J., 2017, Composition of the low seismic velocity E' layer at the top of Earth's core. Geophysical Research Letters, 44(16), 8303-8310, DOI: 10.1002/2017GL074261.

Buffett, B.A., 2010, Chemical stratification at the top of Earth's core: Constraints from observations of nutations. Earth and Planetary Science Letters, 296(3-4), 367-372, DOI: 10.1016/j.epsl.2010.05.020.

Buffett, B.A., and Seagle C.T., 2010, Stratification at the top of the core due to chemical interaction with the mantle. J. Geophys. Res., 115, B04407.

Buffett, B.A., 2014, Geomagnetic fluctuations reveal stable stratification at the top of the Earth's core. Nature, 507, 484-487.

Burke, K., and Torsvik T.H., 2004, Derivation of Large Igneous Provinces of the past 200 million years from long-term heterogeneities in the deep mantle. Earth and Planetary Science Letters, 227(3-4), 531-538, DOI: 10.1016/j.epsl.2004.09.015.

Burke, K., and Torsvik T.H., 2012, Derivation of Large Igneous Provinces of the past 200 million years from long-term heterogeneities in the deep mantle. Earth and Planetary Science Letters, 227(3-4), 531-538, DOI: 10.1016/j.epsl.2004.09.015.

Busse, F.H., 1975, Patterns of convection in spherical shells. Journal of Fluid Mechanics, 72, 67-85, DOI: 10.1017/S0022112075002947.

Cabral, R.A., Jackson M.G., Rose-Koga E.F., Koga K.T., Whitehouse M.J., Antonelli M.A., Farquhar J., Day J.M.D., and Hauri E.H., 2013, Anomalous sulphur isotopes in plume lavas reveal deep mantle storage of Archaean crust. Nature, 496, 490-493.

Campuzano, S.A., De Santis A., Pavón-Carrasco F.J., Osete M.L., and Qamili E., 2018, New perspectives in the study of the Earth's magnetic field and climate connection: The use of transfer entropy. Plos One, 13, 11, Id. e0207270, DOI: 10.1371/journal.pone.0207270.

Campuzano, S.A., Pavón-Carrasco F.J., De Santis A., González-López A., and Qamili E., 2021, South Atlantic Anomaly areal extent as a possible indicator of geomagnetic jerks in the satellite era. Front. Earth Sci., 8, 563, DOI: 10.3389/feart.2020.607049.

Caracas, R., Hirose K., Nomura R., and Ballmer M.D., 2019, Melt-crystal density crossover in a deep magma ocean. Earth Planet. Sci. Lett., 516, 202-211.

Clesi, V., Bouhifd M.A., Bolfan-Casanova N., Manthilake G., Schiavi F., Raepsaet C., Bureau H., Khodja H., and Andrault D., 2018, Low hydrogen contents in the cores of terrestrial planets. Science Advances, 4(3), Id. e1701876, DOI: 10.1126/sciadv.1701876.

Colombi, A., Nissen-Meyer T., Boschi L., and Giardini D., 2014, Seismic waveform inversion for core-mantle boundary topography. Geophys. J. Int., 198, 55-71.

Conrad, C.P., Steinberger B., and Torsvik T.H., 2013, Stability of active mantle upwelling revealed by net characteristics of plate tectonics. Nature, 498(7455), 479-482, DOI: 10.1038/nature12203.

Corgne, A., and Wood B.J., 2005, Trace element partitioning and substitution mechanisms in calcium perovskites. Contrib. Mineral. Petrol., 149, 85-97.

Corgne, A., Liebske C., Wood B.J., Rubie D.C., and Frost D.J., 2005, Silicate perovskite-melt partitioning of trace elements and geochemical signature of a deep perovskitic reservoir. Geochimica et Cosmochimica Acta, 69(2), 485-496, DOI: 10.1016/j.gca.2004.06.041.

Cottaar, S., and Romanowicz B., 2012, An unsually large ULVZ at the base of the mantle near Hawaii. Earth and Planetary Science Letters, 355, 213-222, DOI: 10.1016/j.epsl.2012.09.005.

Courtillot, V., Gallet Y., Le Mouël J-L., Fluteau F., and Genevey A., 2007, Are there connections between the Earth's magnetic field and climate? Earth Planet. Sci. Lett., 253, 3-4, 328-339.

de Koker, N., Steinle-Neumann G., and Vlcek V., 2012, Electrical resistivity and thermal conductivity of liquid Fe alloys at high P and T, and heat flux in Earth's core. Proceedings National Academy of Sciences USA 109, 4070-4073.

de Koker, N., Karki B.B., and Stixrude L., 2013, Thermodynamics of the MgO-SiO_2 liquid system in Earth's lowermost mantle from first principles. Earth and Planetary Science Letters, 361, 58-63, DOI: 10.1016/j.epsl.2012.11.026.

De Santis, A., and Barraclough D.R., 1997, A fractal interpretation of the topography of the scalar geomagnetic scalar potential at the core-mantle boundary, Pure and Applied Geophys., 149, 4, 747-760.

De Santis, A., Barraclough D.R., and Tozzi R., 2003, Spectral and temporal spectra of the geomagnetic field and their scaling properties. Phys. Earth Planet. Int., 135, 125-134.

De Santis, A., Qamili E., Spada G., and Gasperini P., 2012, Geomagnetic South Atlantic Anomaly and global sea level rise: A direct connection? J. Atmos. Sol.-Terr. Phys., 74, 129-135.

De Santis, A., Qamili E., and Cianchini G., 2011, Ergodicity of the recent geomagnetic field. Phys. Earth Plan. Int., 186, 103-110.

De Santis, A., Qamili E., and Wu L., 2013, Toward a possible next geomagnetic transi-tion? Nat. Hazards Earth Syst. Sci., 13, 3395-3403, DOI: 10.5194/nhess-13-3395.

De Santis, A., and Qamili E., 2015, Geosystemics: A Systemic View of the Earth's Magnetic Field and the Possibilities for an Imminent Geomagnetic Transition. Pure Appl. Geophys., 172, 75-89, DOI: 10.1007/s00024-014-0912-x.

Davaille, A., Smrekar S.E., and Tomlinson S., 2017, Experimental and observational evidence for plume-induced subduction on Venus. Nature Geoscience, 10(5), 349-355, DOI: 10.1038/ngeo2928.

Defraigne, P., Dehant V., and Wahr J.M., 1996, Internal loading of a homogeneous compressible Earth with phase boundaries. Geophys. J. Int., 125, 173-192, DOI: 10.1111/j.1365-246X.1996.tb06544.x.

Dehant, V., and Wahr J.M., 1991, The response of a compressible, non-homogeneous Earth to internal loading: Theory. J. Geomagn. Geoelectr., 43, pp. 157-178, DOI: 10.5636/jgg.43.157.

Dehant, V., and Mathews P.M., 2015, Precession, Nutation, and Wobble of the Earth. Cambridge University Press, ISBN: 9781107092549, 536 pages.

Deschamps, F., Rogister Y., and Tackley P.J., 2018, Constraints on core-mantle boundary topography from models of thermal and thermochemical convection. Geophys. J. Int., 212(1), 164-188.

Deuss, A., and Woodhouse J., 2001, Seismic Observations of Splitting of the Mid-Transition Zone Discontinuity in Earth's Mantle. Science, 294(5541), 354-357, DOI: 10.1126/science.1063524.

Dobson, D.P., Lindsay-Scott A., Hunt S.A., Bailey A., Wood I.G., Brodholt J.P., Vocadlo L., and Wheeler J., 2019, Anisotropic diffusion creep in post-perovskite provides a new model for deformation at the core-mantle boundary. Proc. Nat. Acad. Sci., 116, 26389-26393.

Dubrovinsky, L., Dubrovinskaia N., Narygina O., Kantor I., Kuznetzov A., Prakapenka V.B., Vitos L., Johansson B., Mikhaylushkin A.S., Simak S.I., and Abrikosov I.A., 2007, Body-centered cubic iron-nickel alloy in Earth's core. Science, 316, 1880-1883.

Duka, B., Peqini K., De Santis A., and Pavón-Carrasco F.J., 2015, Using "domino" model to study the secular variation of the geomagnetic dipolar moment. Phys. Earth Planet. Inter., 242, 9-23, DOI: 10.1016/j.pepi.2015.03.001.

Dziewonski, A.M., and Anderson D.L., 1981, Preliminary reference Earth model. Phys. Earth Planet. Inter., 25, 297-356.

Faure, P., Bouhifd M.A., Boyet M., Manthilake G., Clesi V., and Devidal J.-L., 2020, Uranium and thorium partitioning in the bulk silicate Earth and the oxygen content of Earth's core. Geochim. Cosmochim. Acta 275, 83-98.

Fei, Y., and Brosh E., 2014, Experimental study and thermodynamic calculations of phase relations in the Fe-C system at high pressure. Earth and Planetary Science Letters, 408, 155-162, DOI: 10.1016/j.epsl.2014.09.044.

Finlay, C.C., Kloss C., Olsen N., Hammer M., Toeffner-Clausen L., Grayver A., et al., 2020, The CHAOS-7 geomagnetic field model and observed changes in the South Atlantic Anomaly. Earth Planets Space, 72, DOI: 10.1186/s40623-020-01252-9.

Ford, H.A., and Long M.D., 2015, A regional test of global models for flow, rheology, and seismic anisotropy at the base of the mantle. Physics of the Earth and Planetary Interiors, 245, 71-75, DOI: 10.1016/j.pepi.2015.05.004.

Forte, A.M., Mitrovica J.X., and Woodward R.L., 1995, Seismic-geodynamic determination of the origin of excess ellipticity of the core-mantle boundary. Earth planet. Sci. Lett., 9(22), 1013-1016.

Forte, A.M., 2007, Constraints on seismic models from other disciplines – Implications for mantle dynamics and composition. In: Treatise on Geophysics, Vol. 1., Elsevier, Eds. A. Dziewonski and B. Romanowicz, 805-858.

Forte, A.M., and Mitrovica J., 2001, Deep-mantle high-viscosity flow and thermochemical structure inferred from seismic and geodynamic data. Nature, 410(6832), 1049-1056.

French, S.W., and Romanowicz B., 2015, Broad plumes rooted at the base of the Earth's mantle beneath major hotspots. Nature, 525(7567), 95-99, DOI: 10.1038/nature14876.

Frost, D.J., and McCammon C.A., 2008, The Redox State of Earth's Mantle. Annual Review of Earth and Planetary Sciences, 36, 389-420, DOI: 10.1146/annurev.earth.36.031207.124322.

Frost, D.J., Asahara Y., Rubie D.C., Miyajima N., Dubrovinsky L.S., Holzapfel C., Ohtani E., Miyahara M., and Sakai T., 2010, The partitioning of oxygen between the Earth's mantle and core. J. Geophys. Res., 115, Id. B02202.

Gallet, Y., Genevey, A., and Fluteau, F., 2005, Does Earth's magnetic field secular variation control centennial climate change? Earth Planet. Sci. Lett., 236, 339-347.

Garnero, E.J., Helmberger D.V., and Grand S.P., 1993, Constraining outermost core velocity with SmKS waves, Geophys. Res. Lett., 20, 2463-2466, DOI: 10.1029/93GL02823.

Garnero, E.J., and McNamara A.K., 2008, Structure and Dynamics of Earth's Lower Mantle. Science, 320(5876), 626, DOI: 10.1126/science.1148028.

Gerya, T.V., Stern R.J., Baes M., Sobolev S.V., and Whattam S.A., 2015, Plate tectonics on the Earth triggered by plume-induced subduction initiation. Nature, 527(7577), 221-225, DOI: 10.1038/nature15752.

Giuliani, A., Jackson M.G., Fitzpayne A., and Dalton H., 2021, Remnants of early Earth differentiation in the deepest mantle-derived lavas. Proceedings of the National Academy of Sciences, 118(1), Id. 2015211118, DOI: 10.1073/pnas.2015211118.

Gizon, L., Cameron R.H., Pourabdian M., Liang Z-C., Fournier D., Birch A.C., and Hanson C.S., 2020, Meridional flow in the Sun's convection zone is a single cell in each hemisphere. Science, 368, 1469-1472.

Glatzmaier, G.A., and Roberts P.H., 1995, A three-dimensional self-consistent computer simulation of a geomagnetic field reversal. Nature, 377, 203-209.

Glatzmaier, G.A., and Roberts P.H., 1996, On the magnetic sounding of planetary interiors, Phys. Earth Planet. Inter. 98, 207-220.

Gomi, H., Ohta K., Hirose K., Labrosse S., Caracas R., Verstraete M.J., and Hernlund J.W., 2013, The high conductivity of iron and thermal evolution of the Earth's core. Phys. Earth Planet. Inter. 224, 88-103.

Gomi, H., and Hirose K., 2015, Electrical resistivity and thermal conductivity of hcp Fe-Ni alloys under high pressure: Implications for thermal convection in the Earth's core. Phys. Earth Planet. Inter. 247, 2-10.

Greber, N.D., Dauphas N., Bekker A., Ptáček M.P., Bindeman I.N., and Hofmann A., 2017, Titanium isotopic evidence for felsic crust and plate tectonics 3.5 billion years ago. Science, 357(6357), 1271-1274, DOI: 10.1126/science.aan8086.

Green, D.H., and Ringwood A.E., 1963, Mineral assemblages in a model mantle composition, J. Geophys. Res., 68(3), 937-945, DOI: 10.1029/JZ068i003p00937.

Greenwood, R.C., Barrat J.-A., Miller M.F., Anand M., Dauphas N., Franchi I.A., Sillard P., and Starkey N.A., 2018, Oxygen isotopic evidence for accretion of Earth's water before a high-energy Moon-forming giant impact. Science Advances, 4, Id. eaao5928.

Greff-Lefftz, M., Pais M.A., and Le Mouel J-L., 2004, Surface gravitational field and topography changes induced by the Earth's fluid core motions. J. Geodesy., 78, 386-392.

Gubbins, D., and Davies C.J., 2013, The stratified layer at the core-mantle boundary caused by barodiffusion of oxygen, sulphur and silicon. Physics of the Earth and Planetary Interiors, 215, 21-28, DOI: 10.1016/j.pepi.2012.11.001.

Gwinn, C.R., Herring T.A., and Shapiro I.I., 1986, Geodesy by radio interferometry: Studies of the forced nutations of the Earth: 2. Interpretation. J. Geophys. Res., 91(B5), 4755-4765.

Hager, B.H., Clayton R.W., Richards M.A., Comer R.P., and Dziewonski A.M., 1985, Lower mantle heterogeneity, dynamic topography and the geoid. Nature, 313(6003), 541-545, DOI: 10.1038/313541a0.

Hager, B.H., and Richards M.A., 1989, Long-wavelength variations in Earth's geoid: physical models and dynamical implications. Phil. Trans. R. Soc. Lond., 328(1599), 309-327.

Harrison, D., Burnard P., and Turner G., 1999, Noble gas behaviour and composition in the mantle: constraints from the Iceland Plume. Earth and Planetary Science Letters, 171(2), 199-207, DOI: 10.1016/S0012-821X(99)00143-0.

Hart, S.R., 1984, A large-scale isotope anomaly in the Southern Hemisphere mantle. Nature, 309(5971), 753-757, DOI: 10.1038/309753a0.

Hazen, R.M., 1999, The Diamond Makers. Cambridge University Press, New York.

Helffrich, G., and Kaneshima S., 2010, Outer-core compositional stratification from observed core wave speed profiles. Nature, 468(7325), 807-810, DOI: 10.1038/nature09636.

Helffrich, G., Hirose K., and Nomura R., 2020, Thermodynamical modeling of liquid Fe-Si-Mg-O: molten magnesium silicate release from the core. Geophysical Research Letters, 47(21), Id. e89218, DOI: 10.1029/2020GL089218.

Hernlund, J.W., and Jellinek A.M., 2010, Dynamics and structure of a stirred partially molten ultralow-velocity zone. Earth and Planetary Science Letters, 296(1-2), 1-8, DOI: 10.1016/j.epsl.2010.04.027.

Hernlund, J.W., and McNamara A.K., 2015, The Core-Mantle Boundary Region. In: Treatise on Geophysics (Second Edition), Elsevier, Ed. G. Schubert, 7.11, 461-519, DOI: 10.1016/B978-0-444-53802-4.00136-6.

Herzberg, C., Condie K., and Korenaga J., 2010, Thermal history of the Earth and its petrological expression. Earth and Planetary Science Letters, 292(1-2), 79-88, DOI: 10.1016/j.epsl.2010.01.022.

Herzberg, C., Vidito C., and Starkey N.A., 2016, Nickel-cobalt contents of olivine record origins of mantle peridotite and related rocks. American Mineralogist, 101(9), 1952-1966, DOI: 10.2138/am-2016-5538.

Hide, R., 1977, Towards a Theory of Irregular Variations in the Length of the Day and Core-Mantle Coupling. Philosophical Transactions for the Royal Society of London. Series A, Mathematical and Physical Sciences, 284(1326), 547-554, DOI: 10.1098/rsta.1977.0030.

Hide, R., and Horai K., 1968, On the topography of the core-mantle interface. Phys. Earth Planet. Inter., 1(5), 305-308.

Hirose, K., Shimizu N., van Westrenen W., and Fei Y., 2004, Trace element partitioning in Earth's lower mantle and implications for geochemical consequences of partial melting at the core-mantle boundary. Physics of the Earth and Planetary Interiors, 146, 249-260.

Hirose, K., Takafuji N., Sata N., and Ohishi Y., 2005, Phase transition and density of subducted MORB crust in the lower mantle. Earth Planet. Sci. Lett., 237, 239-251.

Hirose, K., Labrosse S., and Hernlund J.W., 2013, Composition and State of the Core. Annual Review of Earth and Planetary Sciences, 41, 657-691, DOI: 10.1146/annurev-earth-050212-124007.

Hirose, K., Morard G., Sinmyo R., Umemoto K., Hernlund J., Helffrich G., and Labrosse S., 2017a. Crystallization of silicon dioxide and compositional evolution of the Earth's core. Nature, 543, 99-102.

Hirose, K., Sinmyo R., and Hernlund J., 2017b, Perovskite in Earth's deep interior. Science, 358(6364), 734-738, DOI: 10.1126/science.aam8561.

Hirschmann, M.M., Bergin E.A., Blake G.A., Ciesla F.J., and Li J., 2021, Early volatile depletion on planetesimals inferred from C-S systematics of iron meteorite parent bodies. Proc. Natl. Acad. Sci. USA, 118(13), Id. e2026779118, DOI: 10.1073/pnas.2026779118

Holzapfel, C., Rubie D.C., Mackwell S., and Frost D.J., 2003, Effect of pressure on Fe-Mg interdiffusion in $(Fe_xMg_{1-x})O$, ferropericlase. Physics of the Earth and Planetary Interiors, 139(1-2), 21-34, DOI: 10.1016/S0031-9201(03)00142-0.

Holzapfel, C., Rubie D.C., Frost D.J., and Langenhorst F., 2005, Fe-Mg Interdiffusion in $(Mg,Fe)SiO_3$ Perovskite and Lower Mantle Reequilibration. Science, 309(5741), 1707-1710, DOI: 10.1126/science.1111895.

Irifune, T., and Tsuchiya T., 2015, Phase transitions and mineralogy of the lower mantle. In: Treatise of Geophysics, Ed. G. Schubert, Volume 2 – Mineralogy of the Earth, Chapter 2.03, 33-60.

Irving, J.C.E., Cottaar S., and Lekić V., 2018, Seismically determined elastic parameters for Earth's outer core. Science Advances, 4(6), Id. eaar2538, DOI: 10.1126/sciadv.aar2538.

Ishii, M., and Tromp J., 1999, Normal-Mode and Free-Air Gravity Constraints on Lateral Variations in Velocity and Density of Earth's Mantle. Science, 285(5431), 1231-1236, DOI: 10.1126/science.285.5431.1231.

Ishii, M., and Tromp J., 2001, Even-degree lateral variations in the mantle constrained by free oscillations and the free-air gravity anomaly, Geophys. J. Int., 1(145), 77-96.

Ishii, T., Shi L., Huang R., Tsujino N., Druzhbin D., Myhill R., Li Y., Wang L., Yamamoto T., Miyajima N., Kawazoe T., Nishiyama N., Higo Y., Tange Y., and Katsura T., 2016, Generation of pressures over 40 GPa using Kawai-type multi-anvil press with tungsten carbide anvils. Review of Scientific Instruments, 87, 024501, DOI: 10.1063/1.4941716.

Ito, E., and Takahashi E., 1989, Postspinel transformations in the system Mg_2SiO_4-Fe_2SiO_4 and some geophysical implications. J. Geophys. Res., 94(B8), 10637-10646, DOI: 10.1029/JB094iB08p10637.

Jackson, M.G., Konter J.G., and Becker T.W., 2017, Primordial helium entrained by the hottest mantle plumes. Nature, 542(7641), 340-343, DOI: 10.1038/nature21023.

Jackson, C.R.M., Bennett N.R., Du Z., Cottrell E., and Fei Y., 2018, Early episodes of high-pressure core formation preserved in plume mantle. Nature, 553, 491-495.

Jackson, M.G., Blichert-Toft J., Halldórsson S.A., Mundl-Petermeier A., Bizimis M., Kurz M.D., Price A.A., Harðardóttir S., Willhite L.N., Breddam K., Becker T.W., and Fischer R.A., 2020, Ancient helium and tungsten isotopic signatures preserved in mantle domains least modified by crustal recycling. Proceedings of the National Academy of Sciences, 117(49), 30993-31001, DOI: 10.1073/pnas.2009663117.

Jackson, M.G., Becker T.W., and Steinberger B., 2021, Spatial characteristics of recycled and primordial reservoirs in the deep mantle. Geochem. Geophys. Geosyst., 22, Id. e2020GC009525.

Jamieson, J.C., Lawson A.W., and Nachtrieb N.D., 1959, New device for obtaining x-ray diffraction patterns from substances exposed to high pressure. Rev. Sci. Instrum., 30(11), 1016-1019.

Jault, D., and Le Mouël J., 1990, Core-mantle boundary shape: constraints inferred from the pressure torque acting between the core and the mantle. Geophys. J. Int., 101(1), 233-241.

Jaupart, C., Mareschal J.C., and Iarotsky L., 2016, Radiogenic heat production in the continental crust. LITHOS, 262, 398-427, DOI: 10.1016/j.lithos.2016.07.017.

Kaneshima, S., and Helffrich G., 2013, V_P structure of the outermost core derived from analysing large-scale array data of SmKS waves. Geophysical Journal International, 193(3), 1537-1555, DOI: 10.1093/gji/ggt042.

Kaneshima, S., and Matsuzawa T., 2015, Stratification of Earth's outermost core inferred from SmKS array data. Progress in Earth and Planetary Science, 2, Id. 15, 1-15, DOI: 10.1186/s40645-015-0046-5.

Kaneshima, S., 2018, Array analyses of SmKS waves and the stratification of Earth's outermost core. Physics of the Earth and Planetary Interiors, 276, 234-246, DOI: 10.1016/j.pepi.2017.03.006.

Karlsen, K.S., Domeier M., Gaina C., and Conrad C.P., 2020, A tracer-based algorithm for automatic generation of seafloor age grids from plate tectonic reconstructions. Computers Geosci., 140, 104508.

Kato, C., Umemoto K., Ohta K., Tagawa S., Hirose K., and Ohishi Y., 2020, Stability of fcc phase FeH to 137 GPa. American Mineralogist, 105(6), 917-921, DOI: 10.2138/am-2020-7153.

Kawai, N., and Endo S., 1970, The generation of ultrahigh hydrostatic pressures by a split sphere apparatus. The Review of Scientific Instruments, 41, 1178-1181.

Kennett, B.L.N., 2021, The relative behaviour of bulk and shear modulus as an indicator of the iron spin transition in the lower mantle. Earth and Planetary Science Letters 559, 116808.

Khan, A., Liebske C., Rozel A., Rivoldini A., Nimmo F., Connolly J. A. D., Plesa A. -C., and Giardini D., 2018, A Geophysical Perspective on the Bulk Composition of Mars. Journal of Geophysical Research: Planets, 123(2), 575-611, DOI: 10.1002/2017JE005371.

Kim, T., Ko B., Greenberg E., Prakapenka V., Shim S.-H., and Lee Y., 2020, Low melting temperature of anhydrous mantle materials at the core-mantle boundary. Geophysical Research Letters, 47, e2020GL089345.

Kloss, C., and Finlay C.C., 2019, Time-dependent low-latitude core flow and geomagnetic field acceleration pulses. Geophys. J. Int., 217, 1, 140-168, DOI: 10.1093/gji/ggy545.

Knibbe, J.S., Luginbuehl S.M., Stoevelaar R., van der Plas W., van Harlingen D.M., Rai N., Steenstra E.S., van der Geer R., and van Westrenen W., 2018, Calibration of a multi-anvil high-pressure apparatus to simulate planetary interior conditions. EPJ Techniques and Instrumentation, 5(5), DOI: 10.1140/epjti/s40485-018-0047-z.

Koelemeijer, P., Ritsema J., Deuss A., and van Heijst H.J., 2016, SP12RTS: a degree-12 model of shear- and compressional wave velocity for Earth's mantle. Geophysical Journal International, 204(2), 1024-1039.

Koelemeijer, P., Deuss A., and Ritsema J., 2017, Density structure of Earth's lowermost mantle from Stoneley mode splitting observations. Nature Communications, 8(1), Id. 15241.

Korenaga, J., 2013, Initiation and Evolution of Plate Tectonics on Earth: Theories and Observations. Annual Review of Earth and Planetary Sciences, 41, 117-151, DOI: 10.1146/annurev-earth-050212-124208.

Krasnoshchekov, D., Ovtchinnikov V., and Polishchuk V., 2019, Dissimilarity of the Earth's Inner Core Surface Under South America and Northeastern Asia Revealed by Core Reflected Phases. Journal of Geophysical Research (Solid Earth), DOI: 10.1029/2019JB017408.

Laj, C., and Kissel C., 2015, An impending geomagnetic transition? Hints from the past. Front. Earth Sci., 3, 61, DOI: 10.3389/feart.2015.00061.

Laneuville, M., Hernlund J., Labrosse S., and Guttenberg N., 2018, Crystallization of a compositionally stratified basal magma ocean. Physics of the Earth and Planetary Interiors, 276, 86-92, DOI: 10.1016/j.pepi.2017.07.007.

Lassak, T., McNamara A., Garnero E., and Zhong S., 2010, Core-mantle boundary topography as a possible constraint on lower mantle chemistry and dynamics. Earth Planet. Sci. Lett., 289, 232-241.

Lau, H.C.P., Mitrovica J.X., Davis J.L., Tromp J., Yang H.Y., and Al-Attar D., 2017, Tidal tomography constrains Earth's deep-mantle buoyancy. Nature, 551(7680), 321-326, DOI: 10.1038/nature24452.

Lay, T., and Young C.J., 1990, The stably-stratified outermost core revisited. Geophysical Research Letters, 17(11), 2001-2004, DOI: 10.1029/GL017i011p02001.

Lay, T., 2015, The surge of great earthquakes from 2004 to 2014. Earth and Planetary Science Letters, 409, 133-146, DOI: 10.1016/j.epsl.2014.10.047.

Li, X.-D., Giardini D., and Woodhouses J.H., 1991, Large-scale three-dimensional even-degree structure of the Earth from splitting of long-period normal modes, J. Geophys. Res.: Solid Earth, 96(B1), 551-577.

Li, Y., Vočadlo L., Sun T., and Brodholt J.P., 2020, The Earth's core as a reservoir of water. Nature Geoscience, 13(6), 453-458, DOI: 10.1038/s41561-020-0578-1.

Liebske, C., and Frost D.J., 2012, Melting phase relations in the MgO-$MgSiO_3$ system between 16 and 26 GPa: Implications for melting in Earth's deep interior. Earth and Planetary Science Letters, 345, 159-170, DOI: 10.1016/j.epsl.2012.06.038.

Liu, X., and Zhong S., 2015, Constraining mantle viscosity structure for a thermochemical mantle using the geoid observation. Geophys. Geochem. Geosys., 17(3), 895-913.

Liu, J., Li J., Hrubiak R., and Smith J.S., 2016, Origins of ultralow velocity zones through slab-derived metallic melt. Proc. Natl. Acad. Sci. U. S. A., 113, 5547-5551.

Livermore, P.W., Finlay C.C., and Bayliff M., 2020, Recent north magnetic pole acceleration towards Siberia caused by flux lobe elongation. Nature Geoscience, 13, 387-391.

Lock, S.J., Stewart S.T., Petaev M.I., Leinhardt Z., Mace M.T., Jacobsen S.B., and Ćuk M., 2018, The origin of the Moon within a terrestrial synestia. Journal of Geophysical Research: Planets, 123, 910-951, DOI: 10.1002/2017JE005333.

Lynner, C., and Long M.D., 2014a, Lowermost mantle anisotropy and deformation along the boundary of the African LLSVP. Geophysical Research Letters, 41(10), 3447-3454, DOI: 10.1002/2014GL059875.

Lynner, C., and Long M.D., 2014b, Sub-slab anisotropy beneath the Sumatra and circum-Pacific subduction zones from source-side shear wave splitting observations. Geochemistry, Geophysics, Geosystems, 15(6), 2262-2281, DOI: 10.1002/2014GC005239.

Lynner, C., and Long M.D., 2014c, Testing models of sub-slab anisotropy using a global compilation of source-side shear wave splitting data. Journal of Geophysical Research: Solid Earth, 119(9), 7226-7244, DOI: 10.1002/2014JB010983.

Maas, C., and Hansen U., 2015, Effects of earth's rotation on the early differentiation of a terrestrial magma ocean. J. Geophys. Res., 120, 750-7525.

Maas, C., and Hansen U., 2019, Dynamics of a terrestrial magma ocean under planetary rotation: A study in spherical geometry. Earth Planet. Sci. Lett., 513, 81-94.

Mahaffy, P.R., Donahue T.M., Atreya S.K., Owen T.C., and Niemann H.B., 1998, Galileo Probe Measurements of D/H and $^3He/^4He$ in Jupiter's Atmosphere. Space Science Reviews, 84(1-2), 251-263.

Malavergne, V., Siebert J., Guyot F., Gautron L., Combes R., Hammouda T., Borensztajn S., Frost D., and Martinez I., 2004, Si in the core? New high-pressure and high-temperature experimental data. Geochimica et Cosmochimica Acta, 68(20), 4201-4211, DOI: 10.1016/j.gca.2004.04.013.

Malavergne, V., Cordier P., Righter K., Brunet F., Zanda B., Addad A., Smith T., Bureau H., Surblé S., Raepsaet C., Charon E., and Hewins R.H., 2014, How Mercury can be the most reduced terrestrial planet and still store iron in its mantle. Earth and Planetary Science Letters, 394, 186-197, DOI: 10.1016/j.epsl.2014.03.028.

Malavergne, V., Bureau H., Raepsaet C., Gaillard F., Poncet M., Surblé S., Sifré D., Shcheka S., Fourdin C., Deldicque D., and Khodja H., 2019, Experimental constraints on the fate of H and C during planetary core-mantle differentiation. Implications for the Earth. Icarus, 321, 473-485, DOI: 10.1016/j.icarus.2018.11.027.

Mashino, I., Miozzi F., Hirose K., and Morard G., 2019, Melting experiments on the Fe-C binary system up to 255GPa: Constraints on the carbon content in the Earth's core. Earth and Planetary Science Letters 515, 135-144.

Mandea, M., Narteau C., Panet I., and Le Mouël J.L., 2015, Gravimetric and magnetic anomalies produced by dissolution-crystallization at the core-mantle boundary. Journal of Geophysical Research: Solid Earth, 120(9), 5983-6000, DOI: 10.1002/2015JB012048.

Manga, M., 1996a, Mixing of heterogeneities in the mantle: effect of viscosity differences, Geophys. Res. Lett., 23, 403-406.

Manga, M., 1996b, Dynamics of drops in cavity flows: Aggregation of high viscosity ratio drops, J. Fluid Mech., 8, 1732-1737.

Mao, H.K., and Hemley R.J., 1998, New windows on the Earth's deep interior. In: Ultrahigh-Pressure Mineralogy: Physics and Chemistry of the Earth's Deep Interior, Washington, DC, Mineralogical Society of America, Ed. R.J. Hemley, Reviews in Mineralogy, 37, 1-32.

Mao, H.K., Chen X.J., Ding Y., Li B., and Wang L., 2018, Solids, liquids, and gases under high pressure. Rev. Mod. Phys. 90, 015007.

Mashino, I., Miozzi F., Hirose K., Morard G., and Sinmyo R., 2019, Melting experiments on the Fe-C binary system up to 255 GPa: Constraints on the carbon content in the Earth's core. Earth and Planetary Science Letters, 515, 135-144, DOI: 10.1016/j.epsl.2019.03.020.

Mashino, I., Murakami M., Miyajima N., and Petitgirard S., 2020, Experimental evidence for silica-enriched Earth's lower mantle with ferrous iron dominant Bridgmanite. Proceedings of the National Academy of Sciences, 117(45), 27899-27905, DOI: 10.1073/pnas.1917096117.

Mathews, P.M., Herring T.A., and Buffett B.A., 2002, Modeling of nutation and precession: New nutation series for non-rigid Earth and insights into the Earth's interior, J. Geophys. Res., 107(B4), ETG 3-1-ETG 3-26, DOI: 10.1029/2001JB000390.

Matthews, K.J., Maloney K.T., Zahirovic S., Williams S.E., Seton M., and Müller R.D., 2016, Global plate boundary evolution and kinematics since the late Paleozoic. Global and Planetary Change, 146, 226-250, DOI: 10.1016/j.gloplacha.2016.10.002.

McDade, P., Wood B.J., van Westrenen W., Brooker R., Gudmundsson G., Soulard H., Najorka J., and Blundy J., 2002, Pressure corrections for a selection of piston-cylinder cell assemblies. Mineralogical Magazine, 66, 1021-1028.

McDonough, W.F., and Sun S.S., 1995, The composition of the Earth, Chemical Geology, 120(3-4), 223-253, DOI: 10.1016/0009-2541(94)00140-4.

McMahon, M.I., 2020, Synchrotron and FEL Studies of Matter at High Pressures. In: Synchrotron Light Sources and Free-Electron Lasers, Springer, Eds. E. Jaeschke, S. Khan, J. Schneider, and J. Hastings, DOI: 10.1007/978-3-030-23201-6_67

McNamara, A.K., 2019, A review of large low shear velocity provinces and ultra low velocity zones. Tectonophysics, 760, 199-220, DOI: 10.1016/j.tecto.2018.04.015.

Miozzi, F., Morard G., Antonangeli D., Baron M. A., Boccato S., Pakhomova A., Garbarino G., Mezouar M., and Fiquet G., 2020, Eutectic melting of Fe-3 at% Si-4 at% C up to 200 GPa and implications for the Earth's core. Earth and Planetary Science Letters, DOI: 10.1016/j.epsl.2020.116382.

Morard, G., and Katsura T., 2010, Pressure-temperature cartography of Fe-S-Si immiscible system. Geochimica et Cosmochimica Acta, 74(12), 3659-3667, DOI: 10.1016/j.gca.2010.03.025.

Moreira, M.A., Rouchon V., Muller E., and Noriez S., 2018, The xenon isotopic signature of the mantle beneath Massif Central. Geochem. Persp. Lett., 6, 28-32.

Morelli, A., and Dziewonski A.M., 1987, Topography of the core-mantle boundary and lateral homogeneity of the liquid core. Nature, 325, 678-683.

Mundl, A., Touboul M., Jackson M.G., Day J.M.D., Kurz M.D., Lekic V., Helz R.T., and Walker R.J., 2017, Tungsten-182 heterogeneity in modern ocean island basalts. Science, 356(6333), 66-69, DOI: 10.1126/science.aal4179.

Mundl-Petermeier, A., Walker R.J., Jackson M.G., Blichert-Toft J., Kurz M.D., and Halldórsson S.A., 2019, Temporal evolution of primordial tungsten-182 and $^{3}He/^{4}He$ signatures in the Iceland mantle plume. Chemical Geology, 525, 245-259, DOI: 10.1016/j.chemgeo.2019.07.026.

Mundl-Petermeier, A., Walker R.J., Fischer R.A., Lekic V., Jackson M.G., and Kurz M.D., 2020, Anomalous ^{182}W in high $^{3}He/^{4}He$ ocean island basalts: Fingerprints of Earth's core? Geochimica et Cosmochimica Acta, 271, 194-211, DOI: 10.1016/j.gca.2019.12.020.

Murakami, M., Ohishi Y., Hirao N., et al., 2012, A perovskitic lower mantle inferred from high-pressure, high-temperature sound velocity data. Nature, 485, 90-94, DOI: 10.1038/nature11004.

Nakada, M., and Karato S.I., 2012, Low viscosity of the bottom of the Earth's mantle inferred from the analysis of Chandler wobble and tidal deformation. Physics of the Earth and Planetary Interiors, 192, 68-80, DOI: 10.1016/j.pepi.2011.10.001.

Nimmo, F., 2015, Thermal and Compositional Evolution of the Core. In: Treatise on Geophysics (Second Edition), Elsevier, Ed. G. Schubert, 9.08, 201-219.

Nomura, R., Hirose K., Uesugi K., Ohishi Y., Tsuchiyama A., Miyake A., and Ueno Y., 2014, Low core-mantle boundary temperature inferred from the solidus of pyrolite. Science, 343, 522-525.

O'Neill, H.S.C., Canil D., and Rubie D.C., 1998, Oxide-metal equilibria to 2500°C and 25 GPa: implications for core formation and the light component in the Earth's core. J. Geophys. Res., 103, 12239-12260.

Ohta, K., Kuwayama Y., Hirose K., Shimizu K., and Ohishi Y., 2016, Experimental determination of the electrical resistivity of iron at Earth's core conditions. Nature, 534, 95-98.

Olsen, N., and Mandea M., 2008, Rapidly changing flows in the Earth's core. Nature Geosciences, 1(6), 390-394, DOI: 10.1038/ngeo203.

Olson, P., 2016, Mantle control of the geodynamo: Consequences of top-down regulation. Geochemistry, Geophysics, Geosystems, 17(5), 1935-1956, DOI: 10.1002/2016GC006334.

Ozawa, K., Anzai M., Hirose K., Sinmyo R., and Tateno S., 2018, Experimental Determination of Eutectic Liquid Compositions in the MgO-SiO2 System to the Lowermost Mantle Pressures. Geophysical Research Letters, 45(18), 9552-9558, DOI: 10.1029/2018GL079313.

Parsons, B., and Sclater J.G., 1977, An analysis of the variation of ocean floor bathymetry and heat flow with age. Journal of Geophysical Research, 82(5), 803-827, DOI: 10.1029/JB082i005p00803.

Pavón-Carrasco, F.J., Osete M.L., Torta J.M., and De Santis A., 2014, A geomagnetic field model for the Holocene based on archaeomagnetic and lava flow data. Earth and Planetary Science Letters, 388, 98-109, DOI: 10.1016/j.epsl.2013.11.046.

Pavón-Carrasco, F.J., and De Santis A., 2016, The South Atlantic Anomaly: the key for a possible geomagnetic reversal. Front. Earth Sci., 4, 40, DOI: 10.3389/feart.2016.00040.

Pinheiro, K.J., and Travassos J.M., 2010, Impulses of the Geomagnetic Secular Variation (Jerks) at Vassouras Magnetic Observatory detected by Wavelet Analysis. Revista Brasileira de Geofísica, 28(1), 37-46.

Poirier, J.P., 1994, Light elements in the Earth's core: a critical review. Phys. Earth Planet. Inter., 85, 319-337.

Porcelli, D., and Halliday A.N., 2001, The core as a possible source of mantle helium. Earth and Planetary Science Letters, 192(1), 45-56, DOI: 10.1016/S0012-821X(01)00418-6.

Porcelli, D., and Elliott T., 2008, The evolution of He Isotopes in the convecting mantle and the preservation of high $^{3}He/^{4}He$ ratios. Earth Planet. Sci. Lett., 269, 175-185.

Pozzo, M., Davies C., Gubbins D., and Alfe D., 2012, Thermal and electrical conductivity of iron at Earth's core conditions. Nature, 485, 355-358.

Pradhan, G.K., Fiquet G., Siebert J., Auzende A.L., Morard G., Antonangeli D., and Garbarino G., 2015, Melting of MORB at core-mantle boundary. Earth and Planetary Science Letters, 431, 247-255, DOI: 10.1016/j.epsl.2015.09.034.

Qamili, E., De Santis A., Isac A., Mandea M., Duka B., and Simonyan A., 2013, Geomagnetic jerks as chaotic fluctuations of the Earth's magnetic field, Geochem. Geophys. Geosyst., 14, 4, 839-850.

Reimink, J.R., Chacko T., Stern R.A., and Heaman L.M., 2014, Earth's earliest evolved crust generated in an Iceland-like setting. Nature Geoscience, 7(7), 529-533, DOI: 10.1038/ngeo2170.

Rekier, J., Trinh A., Triana S.A., and Dehant V., 2019, Inertial modes in near-spherical geometries. Geophys. J. Int., 216(2), 777-793, DOI: 10.1093/gji/ggy465.

Rekier, J., Triana S.A., Trinh A., and Dehant V., 2020, Inertial modes of a freely rotating ellipsoidal planet and their relation to nutations. The Planetary Science Journal, 1(1), Id. 20, DOI: 10.3847/PSJ/ab93c8.

Ringwood, A.E., 1962a, A model for the upper mantle, J. Geophys. Res., 67(2), 857-867, DOI: 10.1029/JZ067i002p00857.

Ringwood, A.E., 1962b, Mineralogical constitution of the deep mantle, J. Geophys. Res., 67(10), 4005-4010, DOI: 10.1029/JZ067i010p04005.

Rizo, H., Andrault D., Bennett N.R., Humayun M., Brandon A., Vlastelic I., Moine B., Poirier A., Bouhifd M.A., and Murphy D.T., 2019, 182W evidence for core-mantle interaction in the source of mantle plumes. Geochemical Perspective Letters, 11, 6-11, DOI: 10.7185/geochemlet.1917.

Romanowicz, B., 2003, Global mantle tomography: progress status in the past 10 years. Annual Review of Earth and Planetary Sciences, 31(31), 303-328, DOI: 10.1146/annurev.earth.31.091602.113555.

Rubie , D.C., Jacobson S.A., Morbidelli A., O'Brien D.P., Young E.D., de Vries J., Nimmo F., Palme H., and Frost D.J., 2015, Accretion and differentiation of the terrestrial planets with implications for the compositions of early-formed Solar System bodies and accretion of water. Icarus, 248, 89-108, DOI: 10.1016/j.icarus.2014.10.015.

Saikia, A., Frost D.J., and Rubie D.C., 2008, Splitting of the 520-Kilometer Seismic Discontinuity and Chemical Heterogeneity in the Mantle. Science, 319(5869), 1515, DOI: 10.1126/science.1152818.

Sasao, T., Okubo S., and Saito M., 1980, A simple theory on the dynamical effects of a stratified fluid core upon nutational motion of the Earth. In: Nutation and the Earth's Rotation, Proceedings of the Symposium, Kiev, Ukrainian SSR, May 23-28, 1977, D. Reidel Publishing Co., Dordrecht, 165-183.

Schreiber, T., 2000, Measuring Information Transfer. Phys. Rev. Lett., 85, 2, 461-464, DOI: 10.1103/PhysRevLett.85.461.

Shephard, G.E., Houser C.T., Hernlund J.W, Trønnes R.G., and Valencia-Cardona J.J., 2020, Detection of the spin crossover in ferropericlase in the Earth's lower mantle; an interdisciplinary approach. American Geophyical Union, MR027-02, https://agu.confex.com/agu/fm20/meetingapp.cgi/Paper/692138.

Shirey, S.B., and Richardson S.H., 2011, Start of the Wilson Cycle at 3 Ga Shown by Diamonds from Subcontinental Mantle. Science, 333(6041), 434, DOI: 10.1126/science.1206275.

Simmons, N.A., Forte A.M., and Grand S.P., 2009, Joint seismic, geodynamic and mineral physical constraints on three-dimensional mantle heterogeneity: Implications for the relative importance of thermal versus compositional heterogeneity. Geophys. J. Int., 177(5), 1284-1304.

Simmons, N.A., Forte A.M., Boschi L., and Grand S.P., 2010, GyPSuM: A joint tomographic model of mantle density and seismic wave speeds. J. Geophys. Res., 115(B12), CiteID B12310, DOI: 10.1029/2010JB007631.

Sinmyo, R., Hirose K., and Ohishi Y., 2019, Melting curve of iron to 290 GPa determined in a resistance-heated diamond-anvil cell. Earth Planetary Science Letters 510, 45-52.

Smithies, R.H., Lu Y., Kirkland C.L., Johnson T.E., Mole D.R., Champion D.C., Martin L., Jeon H., Wingate M.T.D., and Johnson S.P., 2021, Oxygen isotopes trace the origins of Earth's earliest continental crust. Nature, 592, 70-75, DOI: 10.1038/s41586-021-03337-1.

Sobolev, S.V., and Brown M., 2019, Surface erosion events controlled the evolution of plate tectonics on Earth. Nature, 570(7759), 52-57, DOI: 10.1038/s41586-019-1258-4.

Soldati, G., Boschi L., and Piersanti A., 2003, Outer core density heterogeneity and the discrepancy between PKP and PcP travel time observations, Geophys. Res. Lett., 30, DOI: 10.1029/2002GL016647.

Soldati, G., Boschi L., and Forte A., 2012, Tomography of core-mantle boundary and lowermost mantle coupled by geodynamics, Geophys. J. Int., 189, 730-746.

Soldati, G., Koelemeijer P., Boschi L., and Deuss A., 2013, Constraints on core-mantle boundary topography from normal mode splitting, Geochem. Geophys. Geosyst., 14(5), 1333-1342.

Souriau, A., 2007, Deep Earth structure – the Earth's cores. In Treatise on Geophysics, Vol. 1: Seismology and the Structure of the Earth, ed. G. Schubert, Publ. Elsevier Amsterdam, pp. 655-693.

Sreenivasan, B., and Gubbins D., 2008, Dynamos with weakly convecting outer layers: implications for core-mantle boundary interaction. Geophysical Astrophysical Fluid Dynamics, 102(4), 395-407, DOI: 10.1080/03091920801900047.

Stacey, F., and Loper, D., 2007, A revised estimate of the conductivity of iron alloy at high pressure and implications for the core energy balance. Phys. Earth Planet. Inter. 161, 13-18.

Starkey, N.A., Stuart F.M., Ellam R.M., Fitton J.G., Basu S., and Larsen L.M., 2009, Helium isotopes in early Iceland plume picrites: Constraints on the composition of high $^{3}He/^{4}He$ mantle. Earth and Planetary Science Letters, 277(1-2), 91-100, DOI: 10.1016/j.epsl.2008.10.007.

Steenstra, E.S., Knibbe J.S., Rai N., and van Westrenen W., 2016, Constraints on core formation in Vesta from metal-silicate partitioning of siderophile elements. Geochimica et Cosmochimica Acta, 177, 48-61.

Steenstra, E.S., and van Westrenen W., 2018, A synthesis of geochemical constraints on the inventory of light elements in the core of Mars. Icarus, 315, 69-78.

Steenstra, E.S., Dankers D., Berndt J., Klemme S., Matveev S., and van Westrenen W., 2019, Significant depletion of volatile elements in the mantle of asteroid Vesta due to core formation. Icarus, 317, 669-681, DOI: 10.1016/j.icarus.2018.08.020.

Steenstra, E.S., and van Westrenen W., 2020, Geochemical constraints on core-mantle differentiation in Mercury and the aubrite parent body. Icarus, 340, 113621.

Steinberger, B., and Torsvik T.H., 2008, Absolute plate motions and true polar wander in the absence of hotspot tracks. Nature, 452(7187), 620-623, DOI: 10.1038/nature06824.

Steinberger, B., and Holme R., 2008, Mantle flow models with core-mantle boundary constraints and chemical heterogeneities in the lowermost mantle. J. Geophys. Res., 113(B5), Id. B05403, DOI: 10.1029/2007JB005080.

Steinberger, B., and Torsvik T.H., 2010, Toward an explanation for the present and past locations of the poles. Geochemistry, Geophysics, Geosystems, 11(6), Id. Q06W06, DOI: 10.1029/2009GC002889.

Stewart, A.J., Schmidt M.W., van Westrenen W., and Liebske C., 2007, Mars: A New Core-Crystallization Regime. Science, 316(5829), 1323, DOI: 10.1126/science.1140549.

Stewart, S.T., Lock S.J., and Caracas R., 2018, Raining a Magma Ocean: Thermodynamics of Rocky Planets After Giant Impacts. 49th Lunar and Planetary Science Conference 19-23 March 2018, The Woodlands, Texas LPI Contribution No. 2083, Id. 1708.

Stixrude, L., de Koker N., Sun N., Mookherjee M., and Karki B.B., 2009, Thermodynamics of silicate liquids in the deep Earth. Earth and Planetary Science Letters, 278(3-4), 226-232, DOI: 10.1016/j.epsl.2008.12.006.

Stixrude, L., and Lithgow-Bertelloni C., 2011, Thermodynamics of mantle minerals – II. Phase equilibria. Geophysical Journal, 184(3), 1180-1213, DOI: 10.1111/j.1365-246X.2010.04890.x.

Stixrude, L., and Lithgow-Bertelloni C., 2012, Geophysics of Chemical Heterogeneity in the Mantle. Annual Review of Earth and Planetary Sciences, 40(1), 569-595, DOI: 10.1146/annurev.earth.36.031207.124244.

Stixrude, L., 2012, Structure of iron to 1 Gbar and 40 000 K. Physical review Letters 108, 055505.

Takafuji, N., Hirose K., Mitome M., and Bando Y., 2005, Solubilities of O and Si in liquid iron in equilibrium with $(Mg,Fe)SiO_3$ perovskite and the light elements in the core. Geophysical Research Letters, 32(6), Id. L06313, DOI: 10.1029/2005GL022773.

Tateno, S., Hirose K., Ohishi Y., and Tatsumi Y., 2010, The Structure of Iron in Earth's Inner Core. Science, 330(6002), 359-361, DOI: 10.1126/science.1194662.

Tateno, S., Hirose K., Komabayashi T., Ozawa H., and Ohishi Y., 2012, The structure of Fe-Ni alloy in Earth's inner core. Geophysical Research Letters, 39(12), Id. L12305, DOI: 10.1029/2012GL052103.

Tateno, S., Hirose K., and Ohishi Y., 2014, Melting experiments on peridotite to lowermost mantle conditions. J. Geophys. Res., 123, 4684-4694.

Tateno, S., Kuwayama, Y., Hirose K., and Ohishi Y., 2015, The structure of Fe–Si alloy in Earth's inner core. Earth and Planetary Science Letters, 418, 11-19.

Tateno, S., Hirose K., Sakata S., Yonemitsu K., Ozawa H., Hirata T., Hirao N., and Ohishi Y., 2018, Melting Phase Relations and Element Partitioning in MORB to Lowermost Mantle Conditions. Journal of Geophysical Research: Solid Earth, 123(7), 5515-5531, DOI: 10.1029/2018JB015790.

Terra-Nova, F., Amit H., Hartmann G.A., Trindade R.I.F., and Pinheiro K.J., 2017, Relating the South Atlantic Anomaly and geomagnetic flux patches, Phys. Earth Planet. Inter., 266, 39-53.

Thébault, E., Finlay C.C., Beggan C.D., et al., 2015, International Geomagnetic Reference Field: the 12th generation, Earth Planets Space, 67, 79, DOI: 10.1186/s40623-015-0228-9.

Thomson, A.R., Crichton W.A., Brodholt J.P., Wood I.G., Siersch N.C., Muir J., Dobson D.P., and Hunt S.A., 2019, Seismic velocities of $CaSiO_3$ perovskite can explain LLSVPs in Earth's lower mantle. Nature, 572, 643-647.

Thorne, M.S., Garnero E.J., and Grand S.P., 2004, Geographic correlation between hot spots and deep mantle lateral shear-wave velocity gradients. Physics of the Earth and Planetary Interiors, 146(1-2), 47-63, DOI: 10.1016/j.pepi.2003.09.026.

Toplis, M.J., Bell J.F., Chassefière E., Sotin C., Spohn T., and Blanc M., 2013a, Quantifying the Martian Geochemical Reservoirs: An Interdisciplinary Perspective. Space Science Reviews, 174(1-4), 5-9, DOI: 10.1007/s11214-012-9951-8.

Toplis, M.J., Mizzon H., Monnereau M., Forni O., McSween H.Y., Mittlefehldt D.W., McCoy T. J., Prettyman T.H., De Sanctis M.C., Raymond C.A., and Russell C.T., 2013b, Chondritic models of 4 Vesta: Implications for geochemical and geophysical properties. Meteoritics Planetary Science, 48(11), 2300-2315, DOI: 10.1111/maps.12195.

Torsvik, T.H., Smethurst M.A., Burke K., and Steinberger B., 2006, Large igneous provinces generated from the margins of the large low-velocity provinces in the deep mantle. Geophysical Journal, 167(3), 1447-1460, DOI: 10.1111/j.1365-246X.2006.03158.x.

Torsvik, T.H., Burke K., Steinberger B., Webb S.J., and Ashwal L.D., 2010, Diamonds sampled by plumes from the core-mantle boundary. Nature, 466(7304), 352-355, DOI: 10.1038/nature09216.

Torsvik, T.H., van der Voo R., Doubrovine P.V., Burke K., Steinberger B., Ashwal L.D., Trønnes R.G., Webb S.J., and Bull A.L., 2014, Deep mantle structure as a reference frame for movements in and on the Earth. Proceedings of the National Academy of Sciences, 111(24), 8735-8740, DOI: 10.1073/pnas.1318135111.

Torsvik, T.H., Steinberger B., Ashwal L.D., Doubrovine P.V., Trønnes R.G., and Polat A., 2016, Earth evolution and dynamics—a tribute to Kevin Burke. Canadian Journal of Earth Sciences, 53(11), 1073-1087, DOI: 10.1139/cjes-2015-0228.

Torsvik, T.H., 2019, Earth history: A journey in time and space from base to top. Tectonophysics, 760, 297-313, DOI: 10.1016/j.tecto.2018.09.009.

Triana, S.A., Rekier J., Trinh A., and Dehant V., 2019, The coupling between inertial and rotational eigenmodes in planets with liquid cores. Geophys. J. Int., 218(2), 1071-1086, DOI: 10.1093/gji/ggz212.

Triana, S.A., Trinh A., Rekier J., Zhu P., and Dehant V., 2020, The viscous and Ohmic damping of the Earth's Free Core Nutation. J. Geophys. Res., accepted.

Trønnes, R.G., 2010, Structure, mineralogy and dynamics of the lowermost mantle. Mineralogy and Petrology, 99(3-4), 243-261, DOI: 10.1007/s00710-009-0068-z.

Trønnes, R.G., Mohn C.E., and Eigenmann K.R., 2018, He and Ne diffusion in bridgmanite and lower mantle structure. Goldschmidt Conf. Abstr. 02d, 0830, We.

Trønnes, R.G., Baron M.A., Eigenmann K.R., Guren M.G., Heyn B.H., Løken A., and Mohn C.E. , 2019, Core formation, mantle differentiation and core-mantle interaction within Earth and the terrestrial planets. Tectonophysics, 760, 165-198, DOI: 10.1016/j.tecto.2018.10.021.

Tsuno, K., Frost D.J., and Rubie D.C., 2013, Simultaneous partitioning of silicon and oxygen into the Earth's core during early Earth differentiation. Geophysical Research Letters, 40(1), 66-71, DOI: 10.1029/2012GL054116.

Umemoto, K., and Hirose K., 2020, Chemical compositions of the outer core examined by first principles calculations. Earth and Planetary Science Letters, 531, Id. 116009, DOI: 10.1016/j.epsl.2019.116009.

Usoskin, I., Korte M., and Kovaltsov G.A., 2008, Role of centennial geomagnetic changes in local atmospheric ionization. Geophys. Res. Lett., 35, L05811.

van der Meer, D.G., Spakman W., van Hinsbergen D.J.J., Amaru M.L., and Torsvik T.H., 2010, Towards absolute plate motions constrained by lower-mantle slab remnants. Nature Geoscience, 3(1), 36-40, DOI: 10.1038/ngeo708.

van der Meer, D.G., van Hinsbergen D.J.J., and Spakman W., 2018, Atlas of the underworld: Slab remnants in the mantle, their sinking history, and a new outlook on lower mantle viscosity. Tectonophysics, 723, 309-448, DOI: 10.1016/j.tecto.2017.10.004.

van Kan Parker, M., Agee C.B., Duncan M.S., and van Westrenen W., 2011a, Compressibility of molten Apollo 17 orange glass and implications for density crossovers in the lunar mantle. Geochimica et Cosmochimica Acta, 75, 1161-1172.

van Kan Parker, M., Mason P.R.D., and van Westrenen W., 2011b, Experimental study of trace element partitioning between lunar orthopyroxene and anhydrous silicate melt: effects of lithium and iron. Chemical Geology, 285, 1-14.

Vasco, D.W., Johnson L.R., and Marques O., 1999, Global Earth structure: inference and assessment, Geophys. J. Int., 137(2), 381-407.

Vocadlo, L., 2015, Earth's Core: Iron and Iron Alloys. Treatise on Geophysics, Ed.: G. Schubert, 2.06, 117-147.

Wade, J., and Wood B.J., 2016, The oxidation state and mass of the Moon-forming impactor. Earth and Planetary Science Letters, 442, 186-193, DOI: 10.1016/j.epsl.2016.02.053.

Walker, D., Carpenter M.A., and Hitch C.M., 1990, Some simplifications to multianvil devices for high pressure experiments. American Mineralogist, 75, 1020-1028.

Walter, M.J., and Trønnes R.G., 2004, Early Earth differentiation. Earth and Planetary Science Letters, 225(3), 253-269, DOI: 10.1016/j.epsl.2004.07.008.

Weir, C.E., Lippincott E.R., Vanvalkenburg A., and Bunting E.N., 1959, Infrared studies in the 1-micron to 15-micron region to 30,000 atmospheres. J. Res. Natl. Bur. Stand. Sect. A Phys. Chem., 63(1), 55-62.

White, W.M., 2015, Isotopes, DUPAL, LLSVPs, and Anekantavada. Chemical Geology, 419, 10-28, DOI: 10.1016/j.chemgeo.2015.09.026.

Wicht, J., and Sanchez S., 2019, Advances in geodynamo modelling. Geophysical Astrophysical Fluid Dynamics, 113(1-2), 2-50, DOI: 10.1080/03091929.2019.1597074.

Wohlers, A., and Wood B.J., 2017, Uranium, thorium and REE partitioning into sulfide liquids: Implications for reduced S-rich bodies. Geochimica et Cosmochimica Acta, 205, 226-244, DOI: 10.1016/j.gca.2017.01.050.

Wolf, A.S., Jackson J.M., Dera P., and Prakapenka V.B., 2015, The thermal equation of state of (Mg, Fe)SiO_3 bridgmanite (perovskite) and implications for lower mantle structures. Journal of Geophysical Research: Solid Earth, 120(11), 7460-7489, DOI: 10.1002/2015JB012108.

Wong, J., Davies C.J., and Jones C.A., 2021, A regime diagram for the slurry F-layer at the base of Earth's outer core. Earth and Planetary Science Letters, DOI: 10.1016/j.epsl.2021.116791.

Wood, B.J., and Kiseeva E.S., 2015, Trace element partitioning into sulfide: How lithophile elements become chalcophile and vice versa. American Mineralogist, 100(11-12), 2371-2379, DOI: 10.2138/am-2015-5358CCBYNCND.

Xia, Y., Kiseeva E.S., Wade J., and Huang F., 2019, The effect of core segregation on the Cu and Zn isotope composition of the silicate Moon. Geochem. Persp. Lett., 12, 12-17.

Yamazaki, D., Ito E., Yoshino T., Tsujino N., Yoneda A., Guo X., Xu F., Higo Y., and Funakoshi K., 2014, Over 1 Mbar generation in the Kawai-type multianvil apparatus and its application to compression of ($Mg_{0.92}Fe_{0.08}$)SiO_3 perovskite and stishovite. Physics of the Earth and Planetary Interiors, 228, 262-267.

Yoshida, M., 2008, Core-mantle boundary topography estimated from numerical simulations of instantaneous mantle flow. Geophys. Geochem. Geosys., 9(7), Id. Q07002, DOI: 10.1029/2008GC002008.

Yoshino, T., Walter M.J., and Tomoo K., 2003, Core formation in planetesimals triggered by permeable flow. Nature, 422(6928), 154-157, DOI: 10.1038/nature01459.

Yuan, K., and Romanowicz B., 2017, Seismic evidence for partial melting at the root of major hot spot plumes. Science, 357(6349), 393-397, DOI: 10.1126/science.aan0760.

Yuan, L., and Steinle-Neumann G., 2020, Strong sequestration of hydrogen into the Earth's core during planetary differentiation. Geophys. Res. Lett., 47, Id. e2020GL088303.

Zhu, P., Triana S.A., Rekier J., Trinh A., and Dehant V., 2020, Quantification of corrections for the main lunisolar nutation components and analysis of the free core nutation remaining in the nutation residuals. Journal of geodesy, submitted.

Acknowledgements

V. Dehant has received funding from the European Research Council (ERC) under the European Union's Horizon 2020 research and innovation programme (GRACEFUL Synergy Grant agreement No 855677). W. van Westrenen

acknowledges funding through a Netherlands Science Organisation (N.W.O.) Vici grant. All the authors would like to thank ISSI for organizing the “Probing the Earth’s Deep Interior Using in Synergy Observations of the Earth’s Gravity and Magnetic Fields, and of the Earth’s Rotation” meeting in these challenging times.